Influence of heavy ionospheric ions on substorm onset

R. M. Winglee[1] and E. Harnett[1]

Received 10 January 2011; revised 6 July 2011; accepted 19 August 2011; published 11 November 2011.

[1] Multifluid/multiscale simulations are used to examine the influence of ionospheric outflows on two substorms that occurred on August 13, 2001. Both substorms had well defined onsets in Cluster ion spectrometer (CIS) data of ion composition of the plasma sheet. It is shown that the model is able to account for two orders of magnitude variation in the H^+ density and one order of magnitude change in the O^+ density in the plasma sheet in association with the ionosphere generating peak outflows of 4×10^{25} H^+ ions/s and 2×10^{25} O^+ ions/s. The model shows that the growth phase is associated with the venting of solar wind plasma in association with the formation of an X-line and the ejection of a plasmoid. This reconnection occurs in a proton-dominated plasma and occurs well before onset. After this venting, a Y-line configuration develops with the ionospheric plasma being the dominant source of the plasma sheet. Lobe reconnection involves heavy enriched O^+ lobe field lines produced by enhanced outflows that start at the beginning of the growth phase. This O^+ produces enhanced dissipation and localized formation of flux ropes prior to substorm onset. For the isolated substorms considered here, the acceleration of O^+ in the plasma sheet keeps the density low in this region but leads to the buildup of both number and density at the inner edge of the plasma sheet. O^+ can contribute nearly 50% of the total energy density in this region just prior to onset. This results in over pressurization and dipolarization in conjunction with onset and associated increases in the nightside auroral currents.

Citation: Winglee, R. M., and E. Harnett (2011), Influence of heavy ionospheric ions on substorm onset, *J. Geophys. Res.*, *116*, A11212, doi:10.1029/2011JA016447.

1. Introduction

[2] Within the near-Earth neutral line substorm model [*Hones*, 1984; *Baker et al.*, 1996] thinning of the plasma sheet in the tail leads to the formation of a magnetic X-line (or magnetic null) at 15–25 R_E (Earth radii) and the ejection of a plasmoid. During this period, the reconnection is occurring within plasma that was originally within the plasma sheet at the start of the growth phase. This type of reconnection is hereafter referred to as plasma sheet reconnection. After the plasmoid ejection, a Y-line neutral line forms in which lobe reconnection occurs. Several papers have argued that substorm onset is associated with reconnection of field lines that were initially in the lobe but convected into the plasma sheet, i.e., lobe reconnection, as opposed to plasma sheet reconnection [*Lyon et al.*, 1998; *Ashour-Abdalla et al.*, 1999]. However, *Ohtani et al.* [2002] have argued that from a study of Geotail observations during substorms that lobe reconnection by itself is not sufficient to drive substorm onset. *Lui et al.* [1991, 1999] have argued that processes at the inner edge of the plasma sheet cause substorm onset. In this paper we investigate the question of why lobe reconnection plays an important role in substorm onset as opposed to plasma sheet reconnection. We demonstrate that ionospheric plasma, and in particular heavy ionospheric ions, play a crucial role in determining substorm onset due to its influence on lobe reconnection, and of equal importance its contributions to the buildup of excess energy density at the inner edge of the plasma sheet.

[3] If lobe reconnection is an important aspect of substorm development then the mass loading of ionospheric plasma on these field lines needs to be understood since the ionosphere is the dominant source of plasma along these field lines. *Baker et al.* [1982] argued that O^+ would increase the growth rate of the linear ion tearing mode in the region $X_{GSM} = -10$ to -15 R_E and $Y_{GSM} \sim 5$ R_E. However, *Shay and Swisdak* [2004] have argued that for a fixed number density the presence of O^+ would lower the Alfvén speed and inhibit the development of the ion tearing mode though the reconnection site itself which show a more layered structure. The problem with these local simulations is that they assume a fixed geometry. Global models [e.g., *Harnett et al.*, 2006] show that both composition and geometry (including thickness) of the plasma are evolving significantly during the growth phase so that the results from a fixed local model are not necessarily applicable as demonstrated in the following.

[4] The outflow of ionospheric plasma into the magnetosphere has been well documented by observations from polar orbiting spacecraft over the last three decades (for reviews

[1]Department of Earth and Space Sciences, University of Washington, Seattle, Washington, USA.

0148-0227/11/2011JA016447

see *Yau and André* [1997], *Peterson et al.* [2001], *Moore et al.* [2001], and *Lotko* [2007]. The derived ionospheric flux derived from these observations indicate outflows to the magnetosphere of 10^{25} and 10^{26} H^+ ions/s and $5 \times 10^{24} - 5 \times 10^{26}$ O^+ ions/s, depending on Kp [*Yau and André*, 1997]. The magnitude of these outflows is sufficiently large that *Chappell et al.* [1987, 2000] proposed that the ionospheric plasma could be a significant source of the plasma sheet and potentially control its dynamics.

[5] The region over which these ionospheric flows dominate the plasma composition is envisaged to extend into at least the mid-tail region, as suggested by single particle tracking [*Delcourt et al.*, 1989, 1993]. Multifluid simulations [*Winglee et al.*, 1998; *Winglee*, 2000] have shown that the region of ionospheric influence changes significantly with solar wind conditions. It is smallest for northward interplanetary magnetic field (IMF) when the polar cap is very small and magnetospheric forcing on the ionosphere is weak. For southward IMF, enhanced heavy ionospheric outflows can be driven by centrifugal forcing associated with increases in the cross-polar cap potential. For these same conditions the entry of solar wind plasma into the magnetosphere is limited to the mantle, with little access to the inner plasma sheet so that plasma of ionospheric origin can dominate the dynamics of the inner to middle magnetosphere during active periods.

[6] A statistical study by *Seki et al.* [1998] showed that within the lobe/mantle O^+ beams between 8 and 210 R_E (Earth radii) have an average density during solar minimum of about 1×10^{-3} cm^{-3}, which corresponds to about 1.2% of the proton component. Even at these low relative concentrations, these heavy ions provide nearly 20% of the mass to the tail, and therefore cannot be considered negligible. Moreover, these heavy ions are seen over much of the magnetosphere, including mid-tail lobe/mantle [*Mukai et al.*, 1994] and the distant tail [*Hirahara et al.*, 1996; *Seki et al.*, 1996]. Thus, if lobe reconnection is playing an important role in substorm development, then the dynamics during this period could be very different from that which would be inferred if the plasma sheet were comprised of entirely H^+.

[7] The transition from plasma sheet (X-line) reconnection to lobe (Y-line) reconnection was recently studied by *Winglee et al.* [2009] using multifluid simulations. They showed that for an idealized substorm the transition from X-line reconnection to Y-line reconnection coincides with the transition of the plasma sheet from having a composition of predominantly solar wind origin to one which is predominantly of ionospheric origin. Substantial fluxes of O^+ can reach the tail and experience preferential acceleration during the later part of the growth phase.

[8] The change in composition of the magnetosphere is particularly important for storms. *Korth et al.* [2002], using CRESS data in the inner magnetosphere, showed that storm-time substorms can have O^+/H^+ ratios of several hundred percent while non-storm-time substorms have O^+/H^+ ratios of 15–65%. In order to remove some of this variability, expansive statistical studies have been developed. *Wilson et al.* [2004] has correlated the outflow rates relative to substorm activity using FAST data between December 1996, and February 1997. They showed that the total nightside auroral zone ion outflow rate increased by a factor of ~10 for both O^+ and H^+ from the smallest to the largest substorms. Irrespective of the storm size, the nightside auroral zone outflow rate increases by about a factor of 2 after onset, and reaches its peak value about 20 min later. Because of this time delay, they noted that the prompt increase of ionospheric ions in the near Earth plasma sheet is likely to come from the local energization of ionospheric ions already present in the magnetosphere.

[9] More recently *Nosé et al.* [2009] examined the influence of storm-time substorms and noted that the flux of ionospheric ions could increase by a factor of 3–50 with a delay of less than several minutes. In the plasma sheet, the flux ratio of O^+/H^+ is rapidly enhanced at the storm-time substorms and then increased gradually or stayed at a constant level in a time scale of 1 h, suggesting a mass-dependent acceleration of ions at local dipolarization and a subsequent additional supply of O^+ ions to the plasma sheet. Similar results for prompt O^+ response have been derived in multifluid simulations of the Oct 29, 2003 Halloween storm [*Harnett et al.*, 2008]. They showed that at the beginning of the event there is a delay between the H^+ and O^+ energization of about 20 min, but after this initial period, prompt acceleration within the magnetosphere of O^+ could account for the observed increases in energetic O^+. The arrival of this O^+ was not balanced by increase fluxes of H^+ so that the O^+ outflows also produced large increases in the ratio of O^+/H^+ in the plasma sheet.

[10] However, *Grande et al.* [2003] have indicated that *Dst* did not appear to have any dependence on the ratio of O^+/He^{++} observed during storms. Furthermore, *Kistler et al.* [2006] have indicated that the plasma sheet during nonstorm substorms does not show any increase in the O^+/H^+ ratio whereas during storm-time substorms the plasma sheet O^+/H^+ density and pressure can increase by as much as factor of 5. They concluded that O^+ does not play a role in nonstorm substorms but could potentially influence storm-time substorms including faster unloading. The change in the ratio of O^+/H^+ during storms could be attributed to either H^+ having a faster depletion rate or O^+ having a faster replenishment rate.

[11] A recent tool that has become available is the development of lists for substorm onsets that were observed in the period 2001–2004. This list was initially developed by *Frey et al.* [2004] who used the FUV instrument on the IMAGE spacecraft to identify over 2400 substorm onsets. *Kistler et al.* [2006] expanded the list of onset to include events identified by injection of energetic particles into the inner magnetosphere so that correlations with onset and Cluster observations in the tail could be made.

[12] In this paper we examine two substorms that are identified in the *Frey et al.* [2004] and *Kistler et al.* [2006] lists that occurred on Aug. 13, 2001. The first substorm identified on this date was an isolated substorm that occurred at 0300 UT (as identified by particle injection) and a second substorm that occurred at 0715 UT as identified by IMAGE. Multifluid/multiscale simulations (section 2) are used to examine the spatial extend of the ionospheric outflows in the magnetosphere and to test whether they can account for the variations in density as seen at by the Cluster Ion Spectrometer (CIS). The ionospheric outflows produced by this model as a function of magnetic local time (MLT) and magnetic latitude (MLat) have been recently validate with respect to both quiet and storm times [*Winglee et al.*,

2008a; *Harnett et al.*, 2008]. The induced ionospheric outflows for the solar conditions are characterized in section 3.

[13] We demonstrate (section 4) that the model is able to account for the presence of high O^+ concentrations in the lobe but the O^+ concentration within the plasma sheet itself remains low for both events, consistent with the results of *Kistler et al.* [2006]. We show that the lack of O^+ concentration in the plasma sheet is due to the preferential acceleration of O^+ and as a result of conservation of flux, the O^+ concentration remains low in the plasma sheet. However, the O^+ energy density at the inner edge of the plasma sheet is seen to increase prior to onset. Onset itself is seen to occur when the energy density of O^+ becomes comparable to the H^+ energy density at the inner edge of the plasma sheet. This increase in O^+ pressure is also shown to occur just prior to the second substorm onset (section 5). These results indicate that ionospheric plasma does play an important role even in isolated substorms.

[14] One difference between the two substorms is that the first substorm has a significantly longer growth phase despite the fact that it occurs during much stronger southward IMF. This difference in growth phase is due to extended access of solar wind plasma to the plasma sheet during a period of rising solar wind dynamic pressure for the first substorm, whereas the solar wind dynamic pressure is smaller and decreasing for the second substorm. This result reinforces the conclusion that ionospheric plasma plays an important role in determining onset.

[15] For both substorms, reconnection signatures occur significantly earlier than onset (section 6). As such while reconnection is necessary for substorm development it is not sufficient for onset. This result is consistent with our earlier simulations of an idealized substorm where X-line reconnection occurs well before onset and leads to the venting of plasma of solar wind origin down the tail. As ionospheric plasma fills this void, a Y-line forms and leads to the injection of energetic plasma into the inner edge of the plasma sheet. Reconnection within the Y-line can be highly localized, leading to earthward and tailward propagating flux ropes. When sufficient energy density/pressure develops at the inner edge of the plasma sheet, onset occurs with auroral brightenings expanding poleward from the equatorward edge of the auroral oval.

[16] A summary of results in given in section 7 with the main conclusion being that despite the fact that the O^+ concentration in the tail might not increase during an isolated substorm, its energy density at the inner edge of the plasma sheet can increase substantially and as such O^+ does play a role in substorm onset even for isolated substorms.

2. Multifluid/Multiscale Modeling

[17] The simulations used in the present study have substantial heritage. The first version of the multifluid code incorporated Hall effects into a 3-D global model using a perturbation expansion [*Winglee*, 1994] valid for $|V \times B| \gg |J \times B|/en$, and provided a first glimpse of how the magnetic topology predicted by MHD would be modified by a small, but nonzero, Hall correction. Because of the ordering of terms with $|V \times B| \gg |J \times B|/en$, this solution was only valid for $V \neq 0$, which is valid in the plasma sheet where strong flows are a persistent feature. The model was subsequently improved to fully incorporate the Hall and ∇P terms without any perturbation approximation, and demonstrated that even at a coarse resolution of 0.25 R_E, these corrections could produce flux ropes with a core magnetic field comparable to observations [*Winglee et al.*, 1998]. The next development of the multifluid model was the incorporation of different sources of various ion species. This work led to the first three dimensional identification of the geopause, as well as a description of the relative roles of ionospheric and solar wind plasma in populating the magnetosphere [*Winglee* 2000], the importance of ionospheric mass outflows in mass loading of the magnetosphere, the generation of the Harang discontinuity, and the cross polar cap potential [*Winglee et al.*, 2002, 2005; *Winglee* 2004]. Excellent agreement with observations has been obtained for weakly magnetized systems such as Mars and Ganymede [*Harnett and Winglee*, 2003, 2007; *Paty and Winglee*, 2004, 2006]. Asymmetric pick-up of heavy ions at Pluto, as seen in hybrid codes but not MHD, has also been demonstrated within the multifluid approach [*Harnett et al.*, 2005]. Comparative studies within the terrestrial magnetosphere have also been successful in quantifying the different populations with the magnetosphere [*Winglee et al.*, 1998; *Li et al.*, 2000] and the development of flux ropes at the magnetopause [*Winglee et al.*, 2008b].

[18] The most recent version of the code incorporates ion skin depth effects in Ohm's law and ion cyclotron terms in the momentum equation that leads to current sheet acceleration [*Winglee et al.*, 2005]. This model has been used to account for the local time variations in ionospheric outflows [*Winglee et al.*, 2008a]. The specifics of the code are as follows. The dynamics of each plasma component are described by mass, momentum and pressure equations given by

$$\frac{\partial \rho_\alpha}{\partial t} + \nabla \cdot (\rho_\alpha \boldsymbol{V}_\alpha) = 0 \tag{1}$$

$$\rho_\alpha \frac{d\boldsymbol{V}_\alpha}{dt} = q_\alpha n_\alpha (\boldsymbol{E} + \boldsymbol{V}_\alpha \times \boldsymbol{B}(\boldsymbol{r})) - \nabla P_\alpha - \left(\frac{GM_E}{R_e^2}\right)\rho_\alpha \vec{\boldsymbol{r}} \tag{2}$$

$$\frac{\partial P_\alpha}{\partial t} = -\gamma \nabla \cdot (P_\alpha \boldsymbol{V}_\alpha) + (\gamma - 1)\boldsymbol{V}_\alpha \cdot \nabla P_\alpha \tag{3}$$

where the subscript α denotes the ion and electron components that constitute the plasma. In hybrid codes and in the multifluid code, one makes the assumption that the electrons are a fluid and that they have sufficiently high mobility along the field lines such that they are approximately in steady state (i.e., $d/dt = 0$) or in drift motion. This assumption removes high frequency plasma waves and electron waves and enables the momentum equation for the electrons to be reduced to

$$\boldsymbol{E} + \boldsymbol{V}_e \times \boldsymbol{B} + \frac{\nabla P_e}{en_e} = 0 \tag{4}$$

[19] The electron dynamics are completed by assuming quasi-neutrality, and applying the definitions for current and electron pressure. For a single component plasma one obtains

$$N_e = N_i, \quad \boldsymbol{V}_e = \boldsymbol{V}_i - \frac{\boldsymbol{J}}{\mathrm{eN_e}}, \quad \boldsymbol{J} = \frac{1}{\mu_0}\nabla \times \boldsymbol{B} \tag{5}$$

$$\frac{\partial P_e}{\partial t} = -\gamma \nabla \cdot (P_e \boldsymbol{V}_e) + (\gamma - 1)\boldsymbol{V}_e \cdot \nabla P_e \quad (6)$$

The magnetic field is obtained by using the electric field (4) in the induction equation

$$\frac{\partial \boldsymbol{B}}{\partial t} + \nabla \times \boldsymbol{E} = 0 \quad (7)$$

[20] In the multifluid treatment, we assume three different ion components: (a) solar wind protons, (b) ionospheric protons, and (c) ionospheric oxygen ions. With these multiple components present, charge and current density are completed by

$$n_e = \sum_i \frac{q_i n_i}{e}, \quad \boldsymbol{V}_e = \sum_i \frac{q_i n_i}{e n_e} \boldsymbol{V}_i - \frac{\boldsymbol{J}}{\mathrm{en_e}}, \quad \boldsymbol{J} = \frac{1}{\mu_0} \nabla \times \boldsymbol{B} \quad (8)$$

Substitution of (8) into (4) yields a modified Ohm's law:

$$\boldsymbol{E} = -\sum_i \frac{q_i n_i}{e n_e} \boldsymbol{V}_i \times \boldsymbol{B} + \frac{\boldsymbol{J} \times \boldsymbol{B}}{e n_e} - \frac{1}{e n_e} \nabla P_e + \eta(x) \boldsymbol{J} \quad (9)$$

The first term in (9) is the ideal Ohm's law. The last term, $\eta(\boldsymbol{x})$ $\boldsymbol{J}$, is added to allow for finite conductivity in the ionosphere only. Collisions beyond this region are assumed to be negligible. No anomalous resistivity is included in the code. Note that the Hall and ∇P_e terms scale with the ratio of the ion skin depth to the current sheet thickness, and becomes important for current sheet thicknesses observed during the latter part of the growth phase. These additional electric fields lead to cross-tail acceleration of heavy ions and the generation of field-aligned currents causing dissipation and the diversion into the ionosphere of some of the cross tail current. The presence of these non-ideal MHD effects allows with physical effects controlling the reconnection including the generation of the core magnetic field that is associated with flux ropes observed in the magnetotail.

[21] If one substitutes the electric field (9) into the ion momentum equation one obtains

$$\rho_\alpha \frac{d\boldsymbol{V}_\alpha}{dt} = q_\alpha n_\alpha \left(\boldsymbol{V}_\alpha \times \boldsymbol{B}(\boldsymbol{r}) - \sum_i \frac{q_i n_i}{e n_e} \boldsymbol{V}_i \times \boldsymbol{B} \right) + q_\alpha n_\alpha \left(\frac{\boldsymbol{J} \times \boldsymbol{B}}{e n_e} - \frac{1}{e n_e} \nabla P_e \right) - \nabla P_\alpha - \left(\frac{GM_E}{R^2} \right) \rho_\alpha \vec{\boldsymbol{r}}. \quad (10)$$

The first term in (10) is dropped in MHD. If this is done and a single species is assumed, (10) reduces to the ideal MHD momentum equation. In reality, the presence of different ion species or energy populations means that the first term is invariably nonzero in weakly magnetized regions but almost zero in strongly magnetized regions. In the weakly magnetized regions the nonzero difference drives ion cyclotron effects, which becomes important when the gyroradius becomes comparable to the scale length of the current sheet.

[22] While the above equations incorporate ion skin depth and ion gyroradius effects, resolving all scale lengths over the entire global system is problematic at best. A tractable solution is obtained by noting that in the strongly magnetized regions around the earth, the particle trajectories derived from particle tracking are consistent with simple convective drift motion and therefore we do not attempt to resolve skin depth and gyroradius effects in these regions [*Winglee*, 2003]. However, in the weakly magnetized regions around the tail and magnetopause current sheets the particle dynamics can differ significantly from MHD treatments where the proton skin depth can be a few hundred kilometers and its gyroradius several hundred kilometers. For O^+, the skin depth can be several hundred kilometers and its gyroradius a few thousand kilometer. At these scale lengths the presence of thin current sheets with a width of 800 km violates the assumptions that are made in formulating the MHD equations. The above multifluid equations with the refinement gridding system outlined below is able to resolve these effects and produces flows that are consistent between the particle and fluid methodologies even in the presence of thin current sheets that form during southward IMF. Under these conditions, ion acceleration as opposed to drift motion occurs whenever the external solar wind conditions lead a current sheet where its thickness is less than about the ion gyroradius [*Winglee*, 2004].

[23] These equations are solved using a second-order Runge-Kutta method with Lapidus smoothing on the above structured grids. The time step is set as the minimum over the grid of the 0.1 $\Delta x/V_{max,}$ and $0.2/\Omega_{i,max}$, where V_{max} is the maximum of the bulk speed, sound speed and Alfvén speeds, and $\Omega_{i,max}$ is the maximum ion cyclotron frequency. The cutoff for the whistler wave that is incorporated within the grid system is dependent on the spatial resolution of the grid. Thus for the coarse grid system the whistler cut off is comparable to the ion cyclotron frequency and the ion plasma frequency is not resolved. In the refined grid system, the ion skin depth is comparable to the grid spacing and the ion plasma frequency has to be resolved. In these regions the Alfvén speed in the lobes is tens of thousands of kilometers per second and sets the time step. Under these conditions, since $\Delta x \sim c/\omega_{pi}$ and $V_A = c\ \Omega_i/\omega_{pi}$ so that the ion plasma frequency is resolved in the reconnection region.

[24] Running high resolution simulations for the global magnetosphere is computationally very expensive. In order to obtain a tractable solution, we first run the code with a stack set of grids. The base resolution is similar to that used in past simulations to set up a 2-h equilibrium for the magnetosphere under quiescent conditions and within which the tail current is relatively thick. The base grid system has a grid spacing of 0.3 R_E in the inner magnetosphere. In the mid- to distant tail, the grid spacing is increased from 0.3 to 2.4 R_E across the nested grids with the largest grid covering in the distant tail to $x \sim -200$ R_E (GSM), and at the flanks at ± 60 R_E with the solar wind boundary is at x = 35 R_E. The inner radius of the simulations is set to 2.7 R_E.

[25] After the above equilibrium is established, the observed IMF conditions are imposed starting about 1 hr prior to the southward turning of the IMF. At the same time refinement gridding is applied to the base grid system of the tail region with a series of overlaying grids giving finer resolution of the tail. Since there is a finite propagation time of the solar wind to the magnetopause and the penetration of fields into the plasma sheet there is more than sufficient time for the current sheet to come into equilibrium with the refinement gridding before the influence of the southward

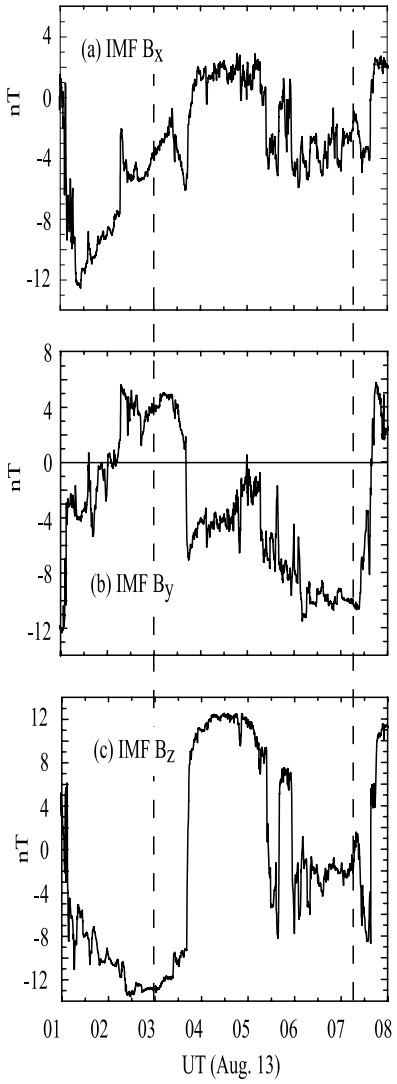

Figure 1. (a–c) The variation of the IMF as a function of time. The IMF conditions have been propagated to the Earth. The dashed lines show the identified onset times which occur at 0300 UT and 0715 UT. The first event is associated with a strong southward IMF while the second event is associated with a slightly negative IMF B_z but with a strong IMF B_y.

IMF is felt. In the present case the resolution is set at 450 km resolution between $-9 < x/R_E < -20$ and y and z between ± 5 R_E, and 900 km for $-1.5 < x/R_E < -33$ and y and z between ± 10 R_E. This resolution is a factor of 4 coarser than used by *Harnett et al.* [2006] but shows the same basic features associated with a very thin current sheet. The coarser resolution allows longer duration simulations and an examination of a great part of parameter space.

[26] The region within the inner boundary is given a finite resistance equivalent to a Reynolds number of 10. At the actual inner boundary (representing the ionosphere), the Reynolds number is increased to 20 and at one grid point above it is set at 40. At all other points the resistivity is zero. These values yield an overall height integrated resistivity of about 10^5 Ohm m^2, which is of the order of the height integrate resistivity of the ionosphere at about 100 km [*Kelley*, 1989]. The corresponding resistance over the auroral zone yields approximately 0.15 mOhm. With the refinement gridding in place dynamics of the reconnection in the tail is predominantly controlled by Hall effects and the composition of the plasma sheet and not by numerical resistivity.

[27] The temperature profile around the inner boundary is also similar to previously published versions of the multifluid model. At the equator, a high temperature of 20 eV is assumed. The plasma temperature then decreases with increasing latitude, reaching a minimum of 0.1 eV at the poles. The high temperature at the equator represents the hotter plasma trapped on closed field lines, while the low temperature over the polar cap is typical for the high latitude ionosphere. The density at the equator is assumed to be 800 cm^{-3}, which is of order of the plasmaspheric density at the radial distance of the inner boundary. Because of the low temperature assumed over the poles, the mobility of the plasma is very small so that we assumed only a slight decrease in density with latitude, with a minimum density at the poles of 400 cm^{-3}. This density is typical of the topside ionosphere over the polar cap. In order to incorporate ionospheric variations associated with changes in magnetosphere activity, the O^+ concentration is set for low magnetospheric activity at 5% concentration at auroral latitudes which then decreases to zero at both the poles and at the equator. This concentration increases proportionally with the total auroral current to a peak concentration of 66% at 25 MA (storm conditions). The total flux yielded by this system gives outflows consistent with *Yau and André* [1997] and with local flux measurements as a function of local time and magnetic latitude [*Winglee et al.*, 2002, 2008a].

3. Solar Wind Conditions and Ionospheric Outflows

[28] Figure 1 shows the variation of the IMF for Aug. 13, 2001. It has been propagated to just in front of the bow shock so that the conditions prior to the observed onset times (dashed) lines can be easily identified. Prior to the time shown there is a period of about three hours in which the IMF is positive with an average value of about 2 nT which leads to a relatively closed magnetosphere where plasma that is primarily of solar wind origin. This configuration is used as the starting point for the present simulations. The first substorm is preceded by a relatively long period of southward IMF which starts at 0110 UT and drops below −5 nT for more than 1 hr 45 min before onset. It reaches its most southward intensity of −12 nT about 30 min prior to onset. This very negative southward IMF is sufficient to drive reconnection in the tail within 30–45 min of the turning within most global magnetospheric models [e.g., *Winglee et al.*, 2009, and references therein] and is true for the present case as well as shown in the following sections. IMF B_z turns more northerly after onset, and as such the paradigm that a northerly turning of the IMF triggers onset does not work in the present case. So while conditions are well suited for the development of a substorm, the actual trigger for onset is inconsistent with many existing paradigms.

[29] For the second substorm onset which occurs at 0715 UT, IMF B_z is slightly southward at between −1 and −2 nT for about an hour prior to onset. A northerly turning occurs about 5 min prior to the observed onset. The fact that

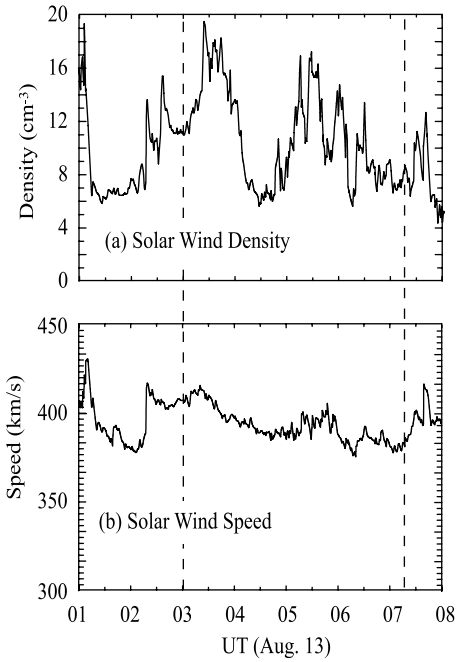

Figure 2. The variations of the solar wind (a) density and (b) speed corresponding to Figure 1. The first substorm is associated with an elevated solar wind density at nearly 12 cm^{-3} and a speed of 410 km/s while the second substorm the solar wind conditions are closer to nominal at ~6 cm^{-3} and 375 km/s.

this substorm has a much shorter growth phase than the first substorm is counterintuitive with respect to the NENL model since the smaller magnitude of IMF B_z is expected to produce a lower reconnection rate. The IMF B_y is the dominant component for the second substorm with an average value of about −10 nT for the hour prior to onset so that there are potentially other drivers for onset.

[30] The corresponding solar wind conditions are shown in Figure 2. The solar wind speed is approximately constant during the preceding hour for each of the substorms, though the speed is higher for the first substorm at ~410 km/s than for the second substorm where the average solar wind speed is about 375 km/s. The average values for V_y is ~40 km/s and V_z is ~− 40 km/s. Because these components are much smaller than V_x they are not imposed on the solar wind conditions but the shift in geometry of the tail of about 5 degrees in taken into account when locating the position of Cluster relative to the center of the plasma sheet. One important different between the substorms is that the solar wind density is rising during the first substorm and declining during the second substorm. This difference as demonstrated in the next section may be a contributing factor to the different duration for the growth phases of the two substorms.

[31] Figure 3 shows the model ionospheric H^+ outflows for the substorm periods in terms of both total flux (Figure 3, middle) and as function of MLT and MLat polar plots (Figure 3, top and bottom). The outflows are measured at a radial distance of 5 R_E and then mapped to the ionosphere to yield fluxes that would be measured at low altitudes [cf. *Winglee et al.*, 2008a]. Since the H^+ density at the inner boundary is fixed, the increases in outflow are due to enhanced forcing from centrifugal acceleration driven by increased polar cap convection potential that accompanies periods of strong southward IMF. For the first substorm with its strong southward IMF the outflows are dominated by the dayside with a total outflow of 4×10^{25} ions/s. The dayside flows have two components: (a) low-latitude component associated with the sunward motion of plasmaspheric plasma and (b) high-latitude component associated with outflows from cusp/cleft region. The low-latitude source provides plasma to the dayside and does not provide a significant source of the plasma to the nightside region which is the focus of the present study. The high-latitude source provides plasma into the distance tail and again does not provide significant plasma to the near-Earth tail. The nightside source which is about a factor of two weaker in total flux but with approximately the same peak flux density is associated with the nightside auroral regions. This source is an important source for the near-Earth plasma sheet. For the second substorm outflows have a similar form but about half the intensity, with a total outflow rate of 2×10^{25} ions/s, and the nightside source fractionally exceeds the dayside source. For both substorms, the ionospheric outflows tend to saturate about 20 min prior to onset.

[32] The corresponding model O^+ outflows are shown in Figure 4. The O^+ outflows for the first substorm do not peak until after about an hour after substorm onset and reach a peak of 2×10^{25} ions/s. Nevertheless, 30 min prior to the first onset the O^+ outflows are nearly a quarter of the H^+ outflow and as such deliver 4 times the mass to the magnetosphere than the H^+ outflows. These outflows are dominated by the dayside in the presence of strong southward IMF B_z. Note that there is no low latitude source as for the case of H^+ since the latter is associated with plasmaspheric processes where there is little O^+. Instead all the O^+ outflows are associated with auroral oval as dayside field lines are convected over the polar cap. For the second substorm the O^+ outflow remains relatively weak at only 2×10^{24} ions/s (or ~10% of the peak outflow rate for the first substorm) since IMF B_z and the corresponding cross polar cap potential are weaker. However, because of the first outflows from the first substorm, O^+ can still be a factor to the dynamics of the magnetosphere during the second substorm.

4. Plasma Density and Composition Variations for the First Substorm

[33] During the period of interest Cluster is at (−17.13 −4.95 −3.37) R_E at 2 UT and is moving slowly earthward reaching (−14.86 −2.97 −5.89) R_E at 7 UT. Figure 5 shows a comparison of the densities observed by the CIS with the densities derived from the simulations. It is seen that the model densities tend to underestimate the observed densities at both the beginning and end of the event A second area where there is some disagreement is between 0530 and 0630 UT where the model proton density exceeds the CIS data by a factor of about 5. This period is 2 1/2 h after the first onset and prior to the growth phase of the second substorm, and is associated with solar wind protons and not ionospheric protons. In other words the discrepancy is not due to issues with the outflow model but associated with the build-up of a cold dense plasma sheet associated with the strong northward IMF that is present after the first substorm.

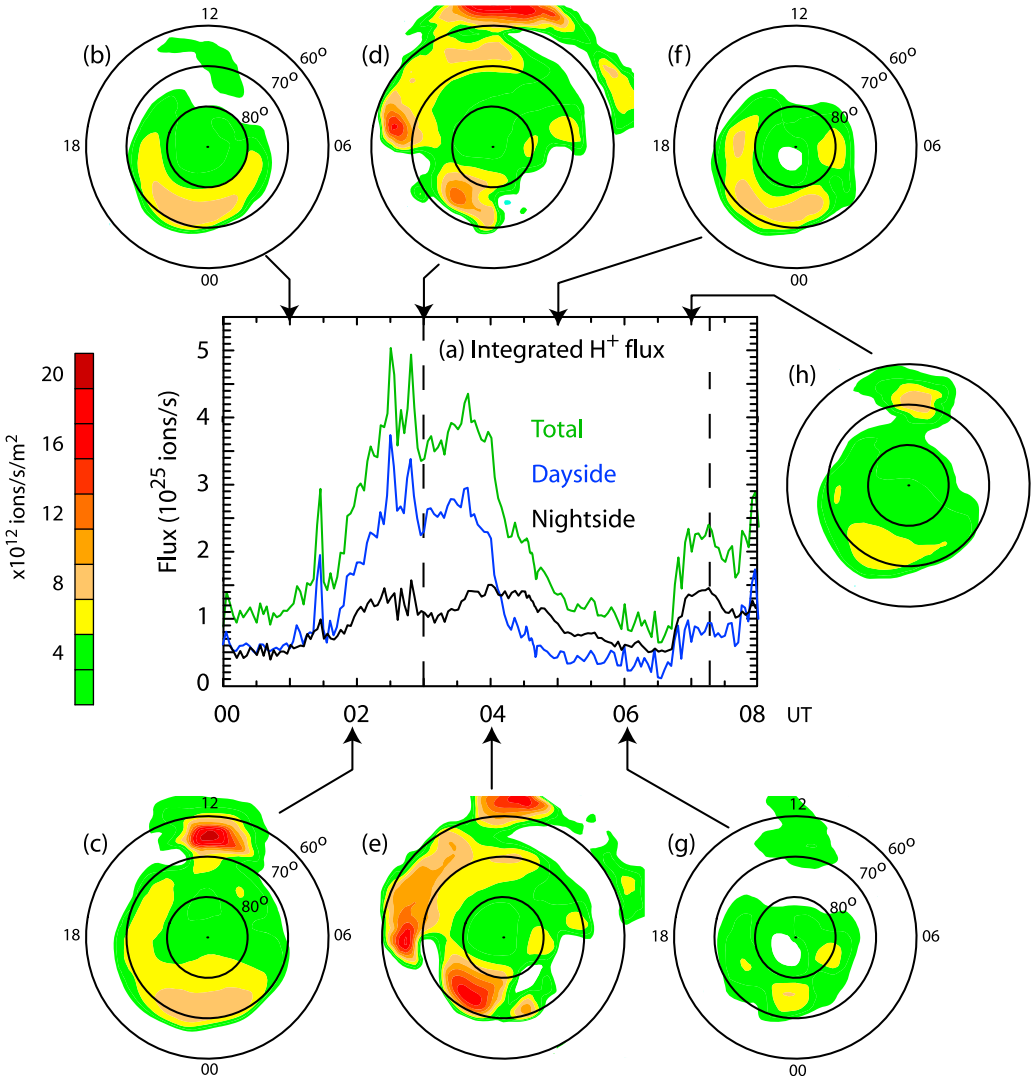

Figure 3. The model H^+ outflows generated by the solar wind conditions in Figures 1 and 2. (a) The integrated flux as a function of time with the dashed lines indicating the observed onset times. (b–h) The outflow as a function of MLT and MLat at selected times. The contouring is set so as to not saturate during the strongest outflows. As a result there are weak outflows across much of the midlatitude regions that do not appear in the contour maps. The strongest outflows of about 4×10^{25} ions/s are associated with the first substorm with the ionospheric outflow being half as small for the second substorm.

Thus, the difference may in fact be that CIS is not seeing these low energy particles as opposed to the model actually over predicting the density. Irrespective of the source of the differences, the model is able to capture the nearly 2 orders of magnitude variation in H^+ and the 1 order of magnitude change in the O^+ density through most of the period of interest, and especially through the growth phase of each of the substorms.

[34] Of equal importance is the fact that the model also captures the relative variation of the density of the two ion species, as seen in Figure 5c. Prior to the development of the growth phase of both events, the relative O^+ density is a few percent consistent with the results of *Seki et al.* [1998]. However, during the growth phase the relative density increases to above 10% for both substorms, despite the fact that the absolute density of both species falls during the growth phase.

[35] In order to gain better insight into variations in the model and CIS data, Figure 6 shows a plot of the CIS data overlaid with the profiles obtained from the model at the average position of Cluster for the period, and at $\Delta Z = \pm 0.6$ R_E from the average position. It is seen that much of the temporal variations seen in the CIS data could be accounted for by overall density profiles obtained by the model with small amount of flapping of the tail between different positions shown. This level of flapping is not resolved in the model and may arise from variations in the solar wind vertical velocity which are neglected in the present work.

[36] The fact that the model is able to account for the CIS observations in terms of both absolute and relative densities for H^+ and O^+ in the tail as well as ionospheric outflows for quiet conditions [*Winglee et al.*, 2008a] means that the model can then be used with confidence to extrapolate the densities between the ionosphere and the tail. Because of the

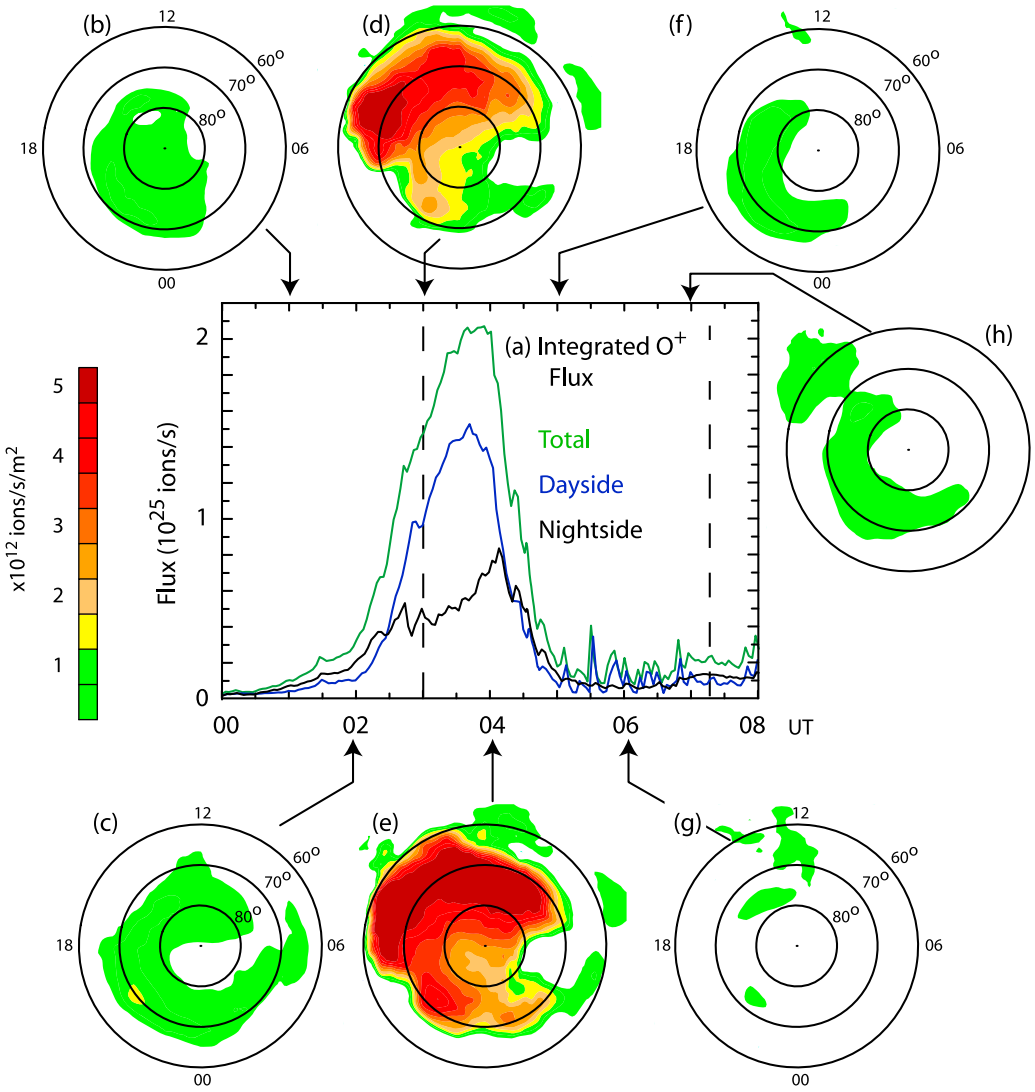

Figure 4. The ionospheric O^+ outflows in the same format as Figure 3. Because of the strong negative IMF B_z, the O^+ outflow reaches a peak of about 2×10^{25} ions/s which is nearly half that of the ionospheric H^+ ions. For the second substorm the outflow remains weak at only about 2×10^{24} ions/s.

complexity of the changes occurring within the magnetosphere we have included in the accompanying auxiliary material four animations with 1 min resolution showing the temporal evolution of 4 key parameters: the total density, the H^+ relative number density, the O^+ relative number density and the O^+ relative energy density.[1] Also included in the auxiliary material are animations of an outward moving flux rope associated with the ejection of the plasmoid, and an earthward moving flux that is present just prior to substorm onset. The details of the development of these fluxes are identical to the idealize case study of *Winglee et al.* [2009] and are not included here to avoid repetition. The following describes key salient features through specific snap shots at discrete times with limited time resolution.

[37] Figure 7 shows the evolution of the total density (Figure 7, left) in the noon-might meridian along with the percent density of ionospheric H^+ of the total proton density (Figure 7, middle) and percent density of the ionospheric O^+ relative to the total number density (Figure 7, right). At the first time shown (as well as preceding times) densities in excess of 5 cm^{-3} are seen at ±1 R_E above the center of the current sheet between −10 and −20 R_E down the tail. At this stage the plasma is primarily of solar wind origin as evidenced by the lack of any significant ionospheric relative density in the tail. By 0157 UT the peak density of the plasma is reduced to ~2 cm^{-3} over a vertical width of <0.3 R_E. This initial thinning occurs around 15 R_E and then spreads both earthward and tailward leaving the current sheet thickness of about ~1200 km between 10 and 20 R_E. This growth phase loss of solar wind plasma down the tail is consistent with the substorm reconfiguration identified by *Winglee et al.* [2009]. The vented solar wind plasma is replaced by ionospheric H^+ at this stage, with a relative density of H^+ reaching 50% of the tail density by 0209 UT. The dominance of ionospheric H^+ occurs well before the identified substorm onset suggests

[1]Auxiliary materials are available in the HTML. doi:10.1029/2011JA016447.

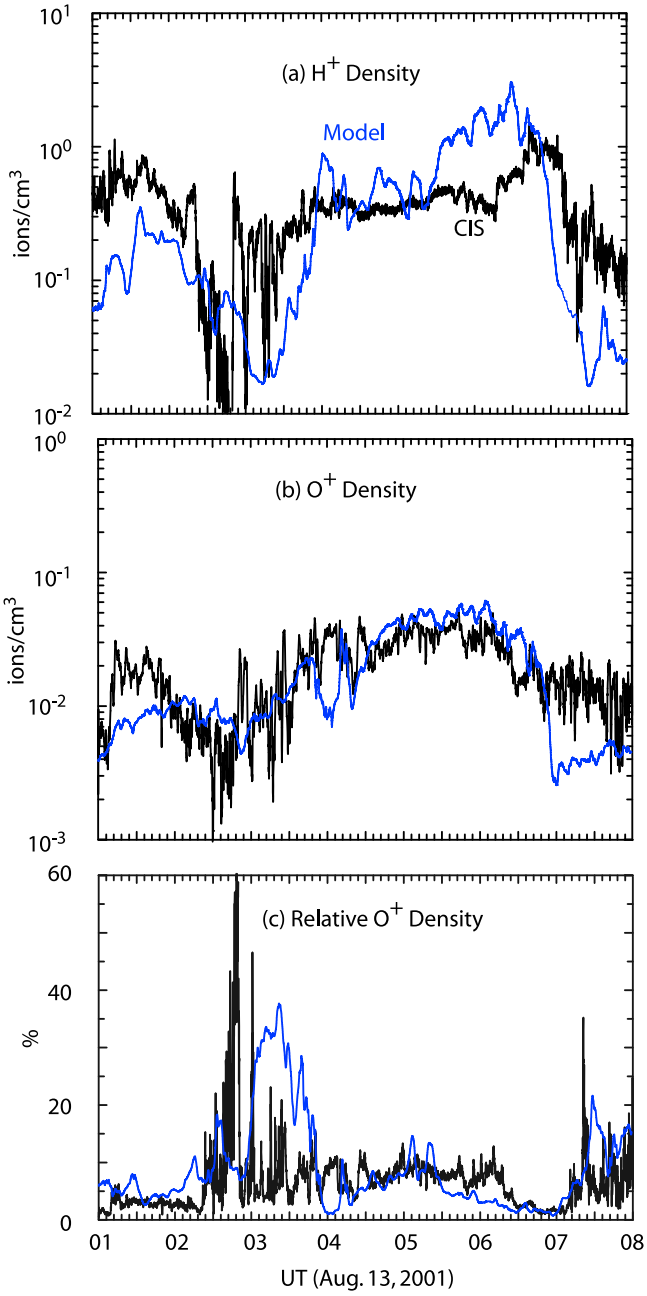

Figure 5. Comparison of the CIS and model densities for (a) H^+ ions, (b) O^+ ions, and (c) the relative O^+ density. The model is able to capture the 2 orders of magnitude variations in H^+ and the 1 order of magnitude variation in O^+, as well as the increase of the relative O^+ density from a few percent during quiet times to well over 10% prior to onset.

that the ionospheric H^+ plasma in important in the growth phase dynamics but the arrival of ionospheric H^+ by itself is insufficient to trigger onset.

[38] The continuation of the evolution of the plasma density and composition up to substorm onset is shown in Figure 8. It is seen that by 0227 UT there are sections of the plasma sheet that are predominantly comprised of ionospheric outflows and in fact there are channels of ionospheric plasma feeding the plasma sheet. Some of this plasma on reaching the plasma sheet is convected earthward as seen by the build of the relative density of ionospheric H^+ at the inner edge of the plasma sheet.

[39] Along with the light ionospheric ions, localized regions of enhanced relative O^+ concentration are seen reaching the tail and Cluster's position shortly after 0237 UT (higher time resolution images show arrival at 0241 UT) and that a portion of this enriched O^+ plasma is accelerated

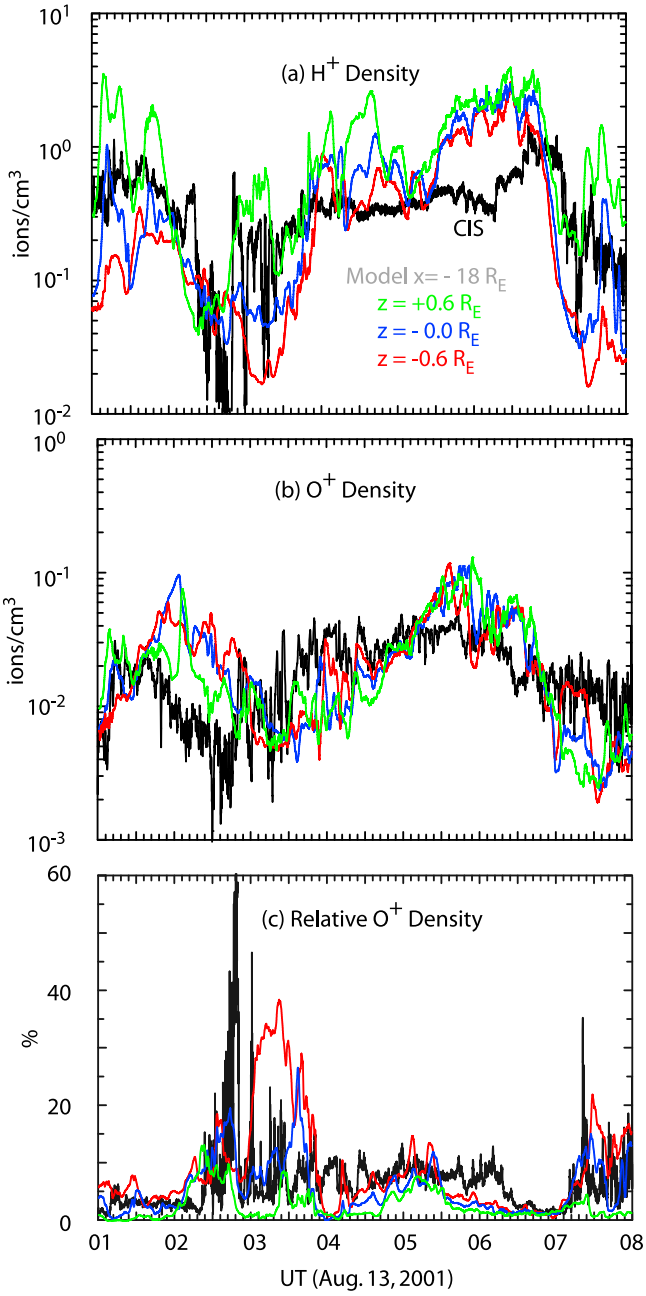

Figure 6. As in Figure 5, except the model densities are for a fixed spacecraft at the mean position of Cluster at x = −16 R_E, y = −4 R_E and z = −4 R_E (blue line) with the red and green lines showing the profiles at a z displacement from this position of −0.6 and +0.6 RE, respectively. In general much of the time variations in the Cluster observations can be accounted by slight vertical motions in z of the current sheet.

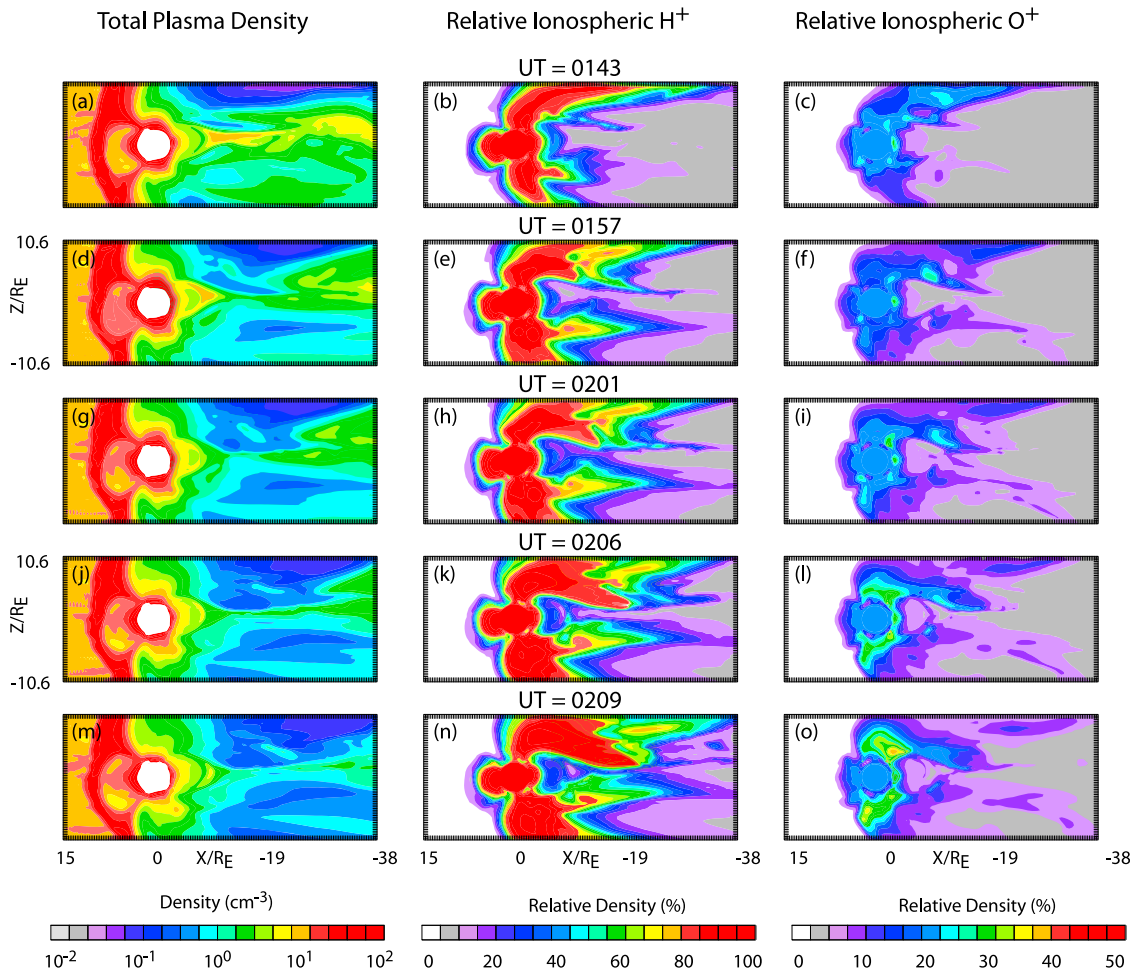

Figure 7. (a–o) Evolution of the (left) total density, (middle) percent ionospheric H^+ density relative to the total proton density and (right) percent O^+ density relative to the total number density for the first half of the growth phase of the first substorm. The cuts are taken along the noon-night meridian. The relative concentration of ionospheric plasma is seen to increase in the lobes which coincides with the loss of solar wind plasma down the tail.

toward the Earth at 0245 UT. On examination of the total density contours it is seen that the enriched regions of O^+ correspond to lower absolute total density, with the ionospheric H^+ reaching further down the tail. These areas dominated by ionospheric ions are lobe-like regions and as demonstrated in the section 6 coincide with the development of lobe reconnection. It should also be noted that the arrival of these regions of enriched O^+ is not continuous but instead is associated with quasiperiodic injections that are seen at 0241 UT and at 0258 UT just prior to onset. The arrival of the first of the O^+ in the plasma sheet is about 15–20 min prior to onset so while the arrival of O^+ is late in the sequence of substorm processes it still arrives prior to onset.

[40] One other feature that is evident in Figure 8 is that the O^+ density in the plasma sheet itself never builds to large concentrations. As such our results are consistent with the results of *Kistler et al.* [2006] who noted no change in the plasma sheet O^+/H^+ density for nonstorm substorms. The big enrichments in O^+ are restricted to the lobes. However, the low O^+ density in the plasma sheet does not mean O^+ is not reaching the plasma sheet. It is quite clear from Figure 8 that such regions are indeed moving into the plasma sheet. The reason that enriched O^+ regions are not present in the plasma sheet is that they experience preferential acceleration there. This preferential acceleration occurs because O^+ has a much larger gyroradius that can exceed the width of the plasma sheet and therefore they can experience direct current sheet acceleration as opposed to the protons which have a higher fraction of their trajectory governed by convective drifts. Because of conservation of flux, the density of O^+ will fall as it is preferentially accelerated. As a result the O^+ density at least for an isolated substorm does not increase in the plasma sheet.

[41] In order to demonstrate that O^+ does have an important role in the energetics of substorm development, Figure 9 shows the total and relative O^+ energy density. The entry point is about 2–3 R_E earthward of Cluster. The energy density profile (Figure 9, left) is very much thinner than the density profiles shown in Figure 8 and is due to the fact that the energization of O^+ is occurring within a thin current sheet. The initial entry point of the enriched O^+ region is indicated by the dashed line and occurs earthward of Cluster's position. This entry point can be seen in the relative O^+ density contours of Figure 8 where the relative

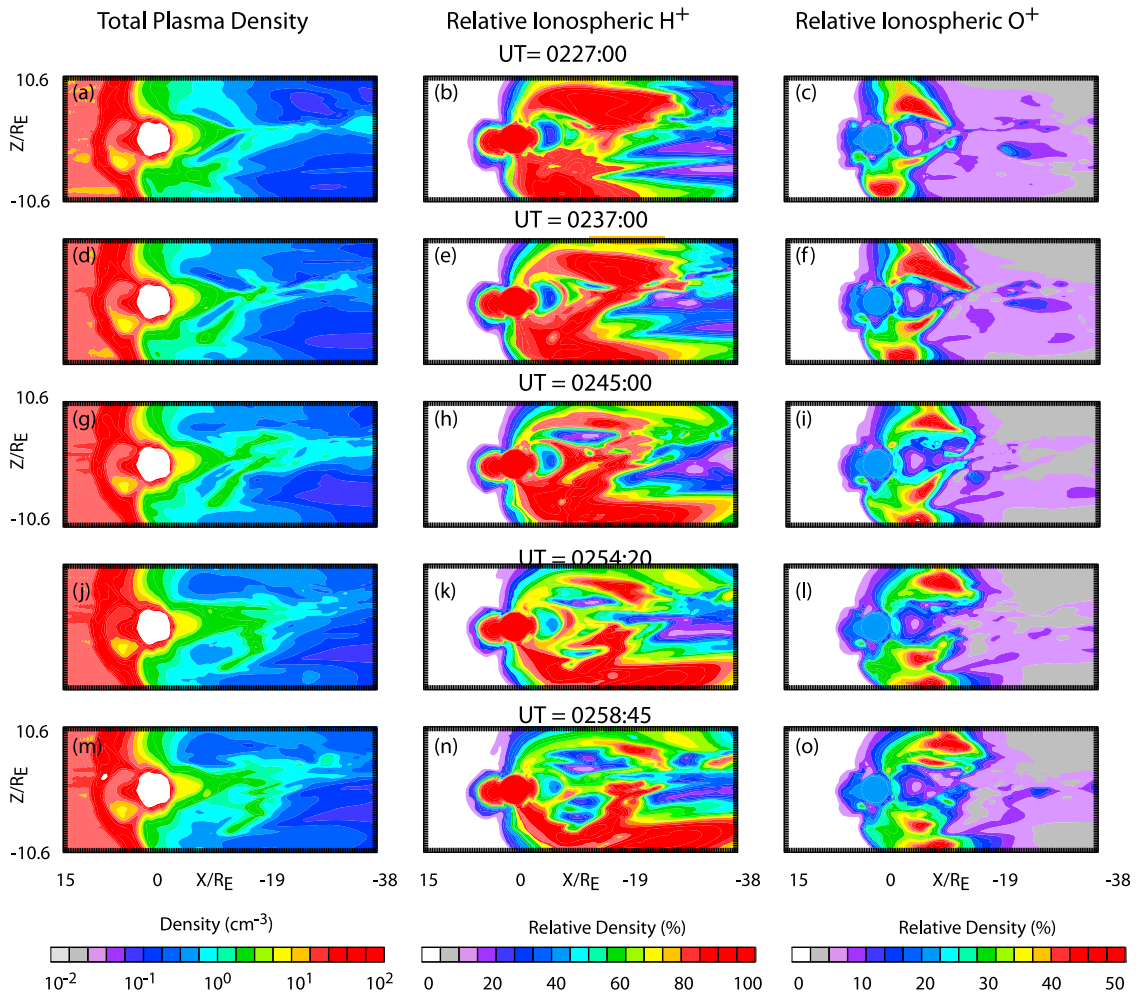

Figure 8. (a–o) Continuation of Figure 7. Ionospheric H^+ dominates the plasma sheet density by 0230 UT but the rising solar wind density seen in Figure 2 leads to some reduction in the dominance of H^+ at late times. O^+ rich regions are also seen to form in the lobes and convect toward the plasma sheet.

density can exceed 10–20% above the plasma sheet entry point. The relative density in the plasma sheet at the entry point shows little or no change in its value. Instead there are enhancements in both the total and relative energy densities, particularly in the northern lobe and in the center of the plasma sheet (Figure 9). A discrete plume of enriched O^+ is seen entering the plasma sheet between 0228 and 0237 UT. Subsequent entry of O^+ is seen to move tailward toward Cluster's position. At the same time some of the energized O^+ is seen to move earthward to the inner edge of the plasma sheet. The relative contribution of O^+ to the total energy density exceeds 60% just prior to onset, which is seen in Figure 9 as a thickening of the plasma sheet starting near the inner edge of the plasma sheet and expanding tailward passed on the O^+ entry point. As noted by *Winglee et al.* [2009] the injection of energetic O^+ can occur via earthward moving flux ropes. These results strongly suggest that O^+ is part of the trigger that leads to substorm onset.

[42] In order to demonstrate that the above changes in the plasma sheet are associated with an auroral substorm, Figure 10 shows the evolution of the model field-aligned currents as a function of MLT and MLat for the northern hemisphere. Because of the relatively strong IMF B_z there are strong dayside currents which start to build at 0100 UT, and do not reach a saturated level until about 0245 UT, which corresponds to the time when significant fluxes O^+ are starting to reach the plasma sheet. At 0249 UT there is a short-lived intensification of the currents between 70 and 80 ILAT and between 23 and 24 MLT. This region of enhanced current moves to the west and declines in intensity over the next 5–7 min producing a pseudo-breakup. These current intensifications are then followed by major current intensifications between 21 and 22 MLT and near 24 MLT which continue for another 45 min (not shown). Thus, the model does in fact indicate auroral current intensifications within minutes of the observed onset.

5. Plasma Density and Composition Variations for the Second Substorm

[43] The hypothesis that O^+ plays a significant role in triggering substorm onset can be tested by considering the second substorm and determining whether the same sequence occurs. This is an important test as the solar wind conditions are very different between the two substorms. As noted in section 3, this second substorm is associated

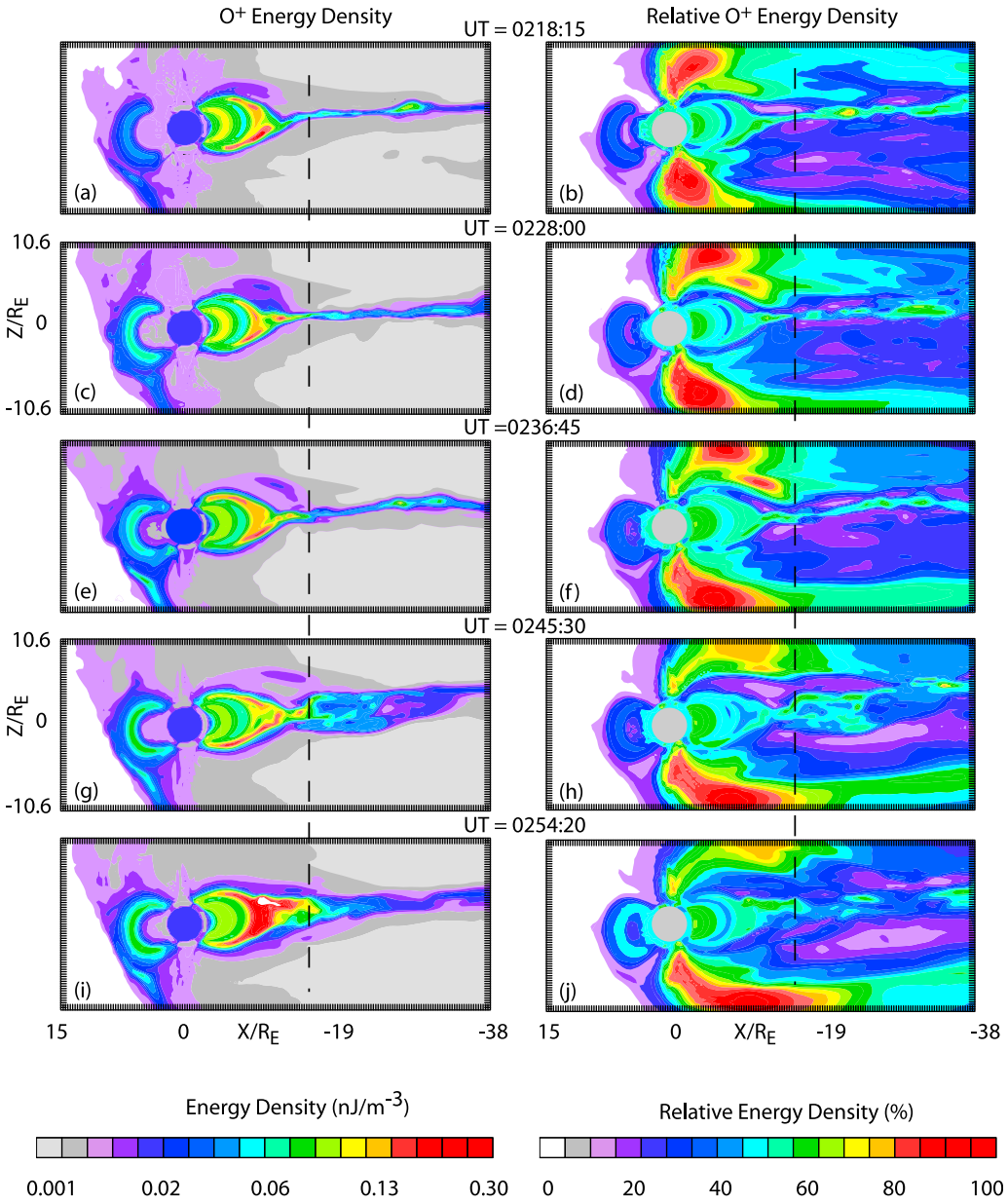

Figure 9. (left) Energy density of O^+ and (right) its relative contribution to the total energy density. The dashed lines show the entry point of enriched O^+ regions entering the plasma sheet. Onset is associated with the build up of the energy density of O^+ at the inner edge of the plasma sheet up to the point where it contributes nearly 50% of the total energy density.

with a lower and declining solar wind density and IMF B_z while negative is relatively weak at ~−2 nT. IMF B_y is enhanced but the magnitude of the IMF is smaller than for the first event. One important difference between these two substorms is that if the growth phase is measured as starting from the beginning of the southward turning (Figure 1) then it is nearly 2 h for the first substorm and only 1 h and 15 min for the second substorm despite the fact that the latter has the weaker IMF B_z.

[44] The reason for the different behavior for the two substorms can be seen in Figure 11 which shows the evolution of the density in the noon-meridian for the second substorm. The lower and declining solar wind density results in a reduction in the total density in the magnetosphere, which can be seen in comparing the total density contours between Figures 6 and 10. As a result, the dominance of ionospheric plasma occurs faster in the second substorm, occurring within 1 hr of the southward turning (as seen in Figure 11 (middle)) while it takes 1 h and 15 min for the first substorm. Of equal significance is that O^+ enriched regions reach the tail within 1 hr and 15 min in the second substorm while it takes nearly 1 h 45 min for the first substorm. This prompt response is because some of the O^+ that is being processed in the second substorm comes from O^+ ejected late in the development of the first substorm. Some of this earlier ejected O^+ is seen to be convected all the way into the inner magnetosphere and can participate in the formation of an almost symmetric ring current. Similar to the first substorm,

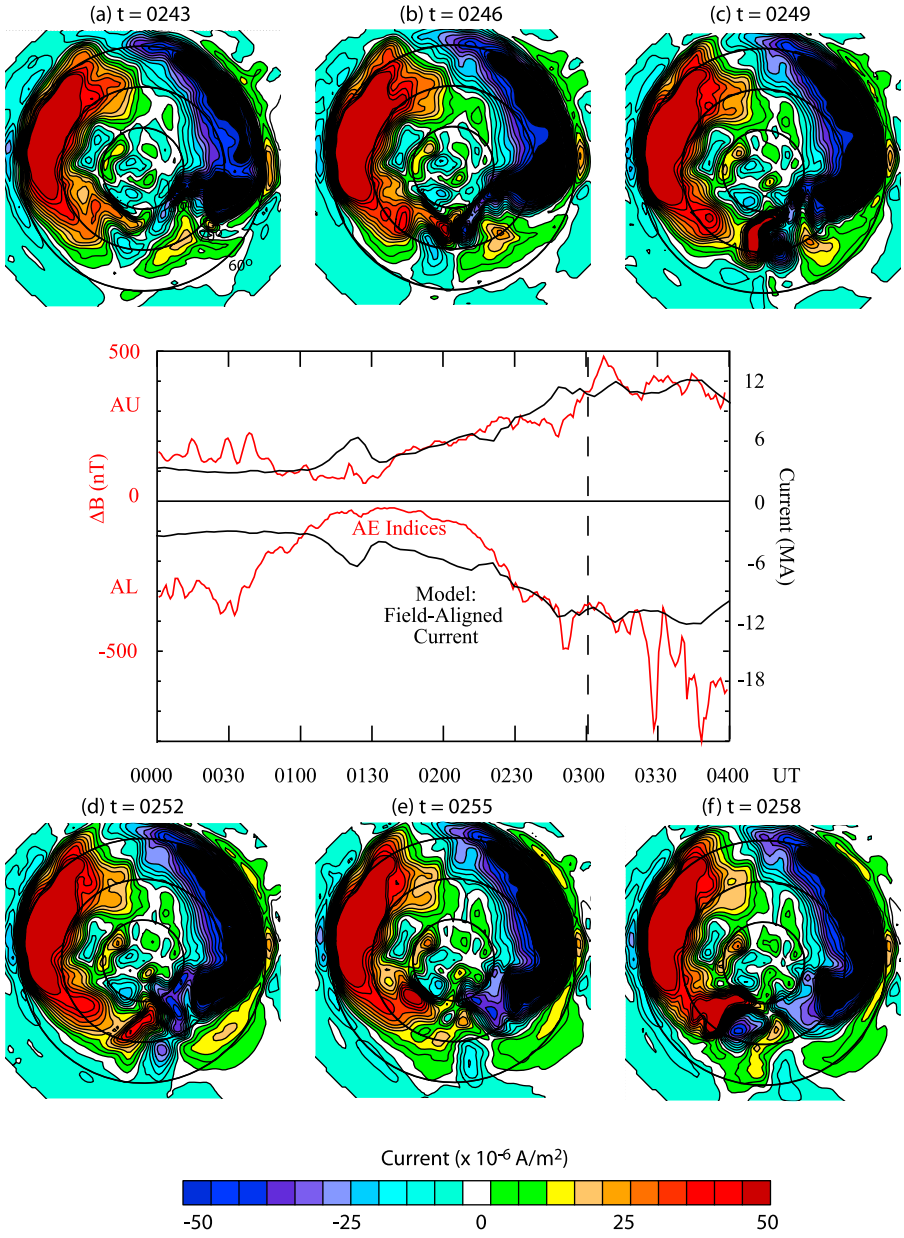

Figure 10. (top and bottom) The development of the model auroral field line currents in the northern hemisphere leading up to the observed substorm onset at 0300 UT. (middle) The total upward and downward currents as a function of time overlaid with the AE index for the event. The AE index provides a reference frame for the changes in the field-aligned currents relative to the storm onset The model results shown a short-lived current intensification near midnight at 0249 UT (pseudo-breakup) with larger and longer lived current intensifications near 22 and 24 MLT at 0258 UT (model onset).

enhanced regions of O^+ are seen in the lobe but the O^+ never becomes the dominant contributor to the density in the plasma sheet.

[45] Prior to onset the current sheet is thinner than the O^+ gyroradius so that O^+ is again a significant contributor to the energy density as illustrated in Figure 12 which shows cuts of the relative O^+ energy density along the noon-midnight meridian and equatorial plane. Because of the activity associated with the first substorm, O^+ is a significant (>50%) contributor to the energy density in the inner magnetosphere, lobes and plasma sheet. The O^+ in the lobe is seen to be converted into the plasma sheet. The northern hemisphere appears to be the dominant source for the mid-tail region while the southern hemisphere loads the tail at slightly larger distances. This asymmetry is due to seasonal/dipole-tilt dependence of the O^+ outflows. These outflows lead to an enhanced O^+ energy density at the inner edge of the plasma sheet, particularly between 0701 and 0708 UT. This build up of O^+ energy density at the inner edge of the plasma sheet is followed by the ejection down the tail of some of the O^+ as seen in Figure 12d at 0716 UT which is near the time of the observed substorm onset.

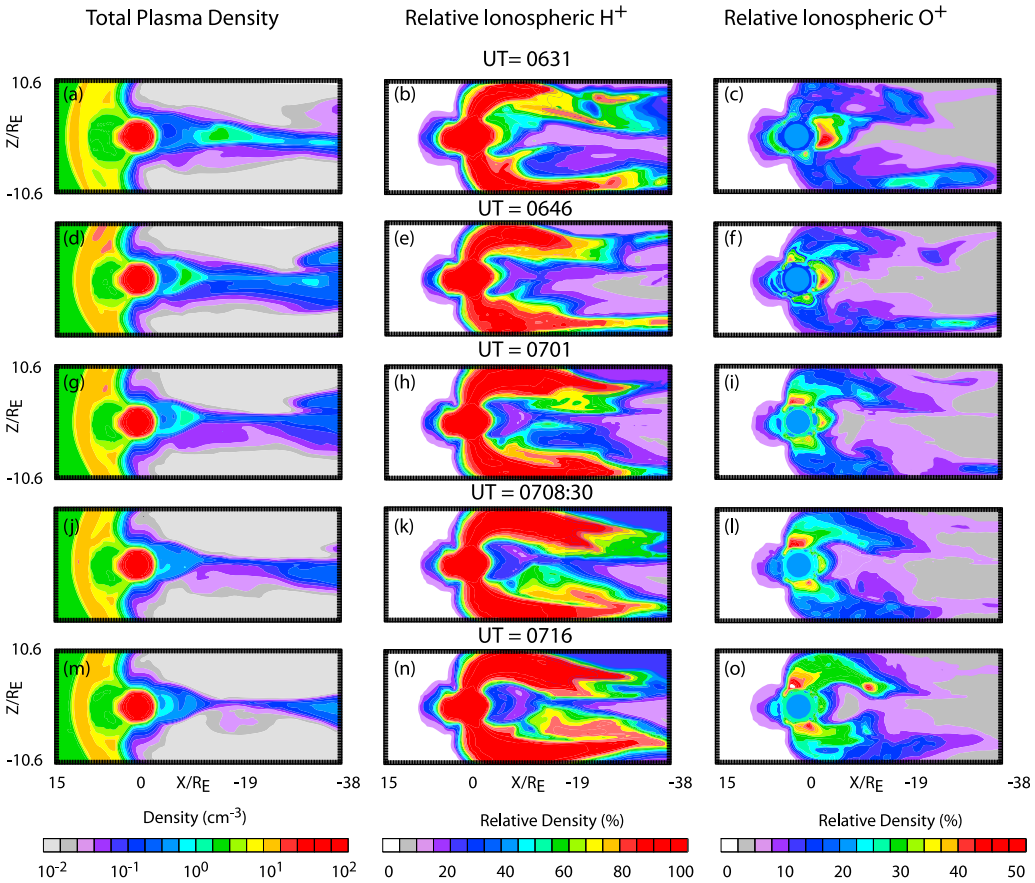

Figure 11. (a–o) Evolution of the (left) total density, (middle) relative ionospheric H^+ density and (right) relative O^+ density in the noon-midnight meridian for the second substorm that occurred on Aug. 13, 2001. While the solar wind conditions are very different between the two substorms, thinning of the plasma occurs about 30 min prior to onset and enhanced ionospheric H^+ concentrations are seen about 15 min prior to onset. Close to onset regions of enhanced O^+ are seen to feed into the plasma sheet.

[46] The development of the corresponding auroral signatures as seen in the field-aligned currents is shown in Figure 13. As with the first substorm the total integrated field-aligned current tracks AU very closely. The intensity of the currents is about half that of the first substorm, which correlates with the reduced IMF B_z for the second substorm. The field-aligned currents around 23 MLT and between 65 and 72 ILAT intensify around 0708 UT, which is about 7 min prior to the observed onset. This intensification is followed by a slight weakening of the midnight currents, which then re-intensify around 0726 UT and reach their peak intensity around 0731 UT. Thus the model also is seeing auroral substorm features within several minutes of the observed onset time.

[47] In summary the model indicates that for both substorms the thinning of the current sheet during the growth phase leads to the reduction of solar wind plasma within the plasma sheet. This plasma is replaced by plasma of ionospheric origin. Regions within the lobe that are enriched in O^+ are convected into the thinned current sheet. This energized O^+ eventually leads to an over pressurization at the inner edge of the plasma sheet which leads to dipolarization and the ejection of some of the excess plasma down the tail. In the next section, we examine the reconnection signatures occurring with the above activity.

6. Reconnection Effects

[48] Reconnection is often taken to be synonymous with substorm onset. Here we show that X-line (plasma sheet) reconnection occurs well before the observed onset and is a growth phase feature and not an onset feature. The development of reconnection for the first substorm during the growth phase is shown in Figure 14. Contours of B_z is shown on the left hand side in the noon-midnight meridian and in the equatorial plane. The green dashed line delineates the transition from positive to negative B_z. The total plasma pressure is shown on the right hand side which gives an indication of the position and thickness of the plasma sheet well as conditions in the lobes and magnetosheath. If the plasma is in approximate equilibrium, then contours of constant plasma pressure in the noon-midnight meridian give an indication of the curvature of the field lines (the actual field lines are not shown as they tend to complicate the figures).

[49] It is seen in Figure 14 that prior to the southward turning on the IMF, the lobe which is seen as low-pressure regions makes a transition from negative to positive B_z at

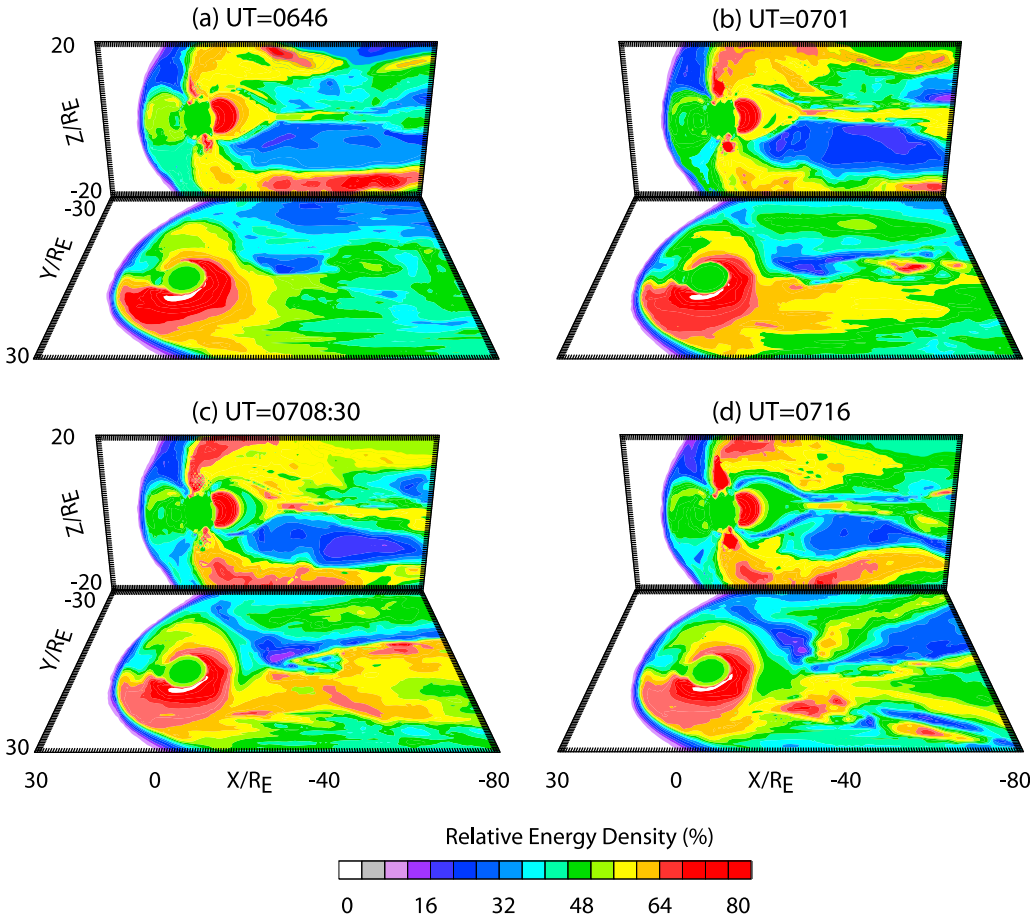

Figure 12. (a–d) Evolution of the relative O^+ energy density in the noon-midnight meridian and equatorial plane prior to the onset of the second substorm. O^+ energized by the first substorm dominates the energy distribution in the inner magnetosphere. At the inner edge of the plasma sheet freshly injected O^+ contributes a majority of the energy and at substorm onset this plasma is ejected down the tail.

around 30 R_E. The southward turning pushes the transition line out to about 70 R_E down the tail. However, in the current sheet the region of strong positive B_z remains in the vicinity of 30 R_E. On the earthward side at about 15–20 R_E, a small region of negative B_z develops at 0152 UT in association with enhanced plasma pressure in the center of the current sheet. This region is seen to expand at 0158 UT, and is the beginning of tail reconnection which is verified by field line mapping (not shown). This reconnection occurs well in advance of the observed substorm onset.

[50] The continuation of the plasma sheet dynamics is shown in Figure 15. A region of $\pm B_z$ is seen to be ejected down the tail. This structure is actually a plasmoid being ejected down the tail. The ejection is also seen in the plasma pressure profiles as a very thick (>5 R_E) bulge in the plasma pressure. The ejection is associated with the formation of an X-line with strong negative B_z extending several R_E above the equatorial plane (e.g., from 0210 to 0228 UT). In the wake of the plasmoid the current sheet is very thin (<0.5 R_E) as seen in the pressure contours and the regions of more intense negative Bz are restricted to the plasma sheet. This type of configuration signifies the development of Y-line reconnection in the post-plasmoid current sheet [cf. *Harnett et al.*, 2006; *Winglee et al.*, 2009].

[51] Along the Y-line there are small budges in the plasma sheet which is associated with the development of small-scale flux ropes which propagate both earthward and tailward from the mid-tail region. These flux ropes are associated with localized reconnection lines as seen in Figure 15g with the formation of a new reconnection line in the mid-tail region. This scenario is identical to that described by *Winglee et al.* [2009] for the development of an idealized substorm. Note that the Y-line forms more than 30 min prior to onset and this reconnection occurs in plasma that is dominated by ionospheric plasma (Figure 8). In other words plasma sheet reconnection occurs several tens of minutes prior to onset and lobe reconnection is initiated a few tens of minutes later but still before onset.

[52] Figure 16 shows tail structure leading up to substorm onset. The magnitude of B_z in the lobes remains low at less than 2 nT indicating the absence of any large magnetic reconnection features. There are however localized regions of reconnection as seen by the presence of $\pm B_z$ pairs of plasma sheet (e.g., 0237 and 0247 UT) which are associated with flux ropes. These flux ropes can propagate tailward as well as earthward. At the actual time of onset there are no strong large-scale reconnection features.

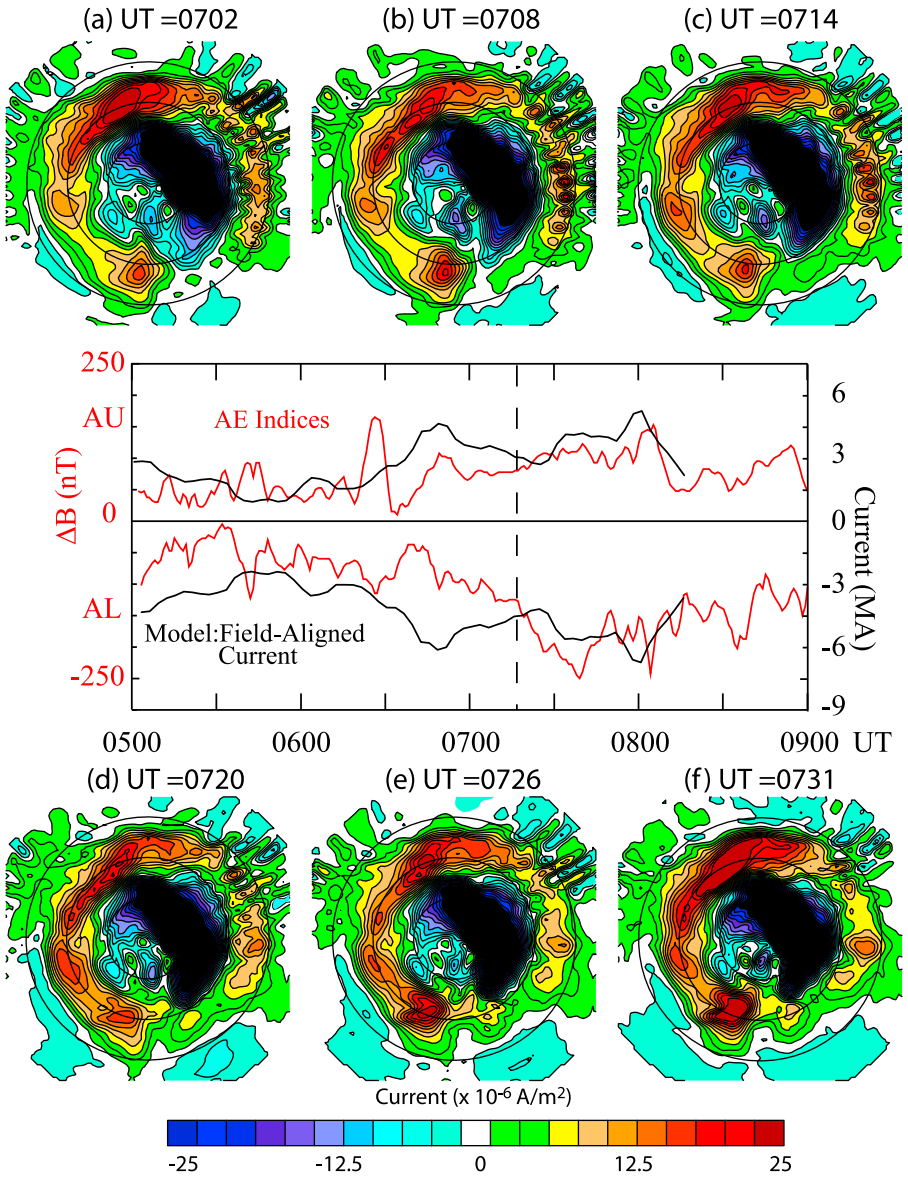

Figure 13. As in Figure 10 except for the second substorm and all scales are half as small. There are two intensifications of the nightside auroral currents at 0708 and 0726 UT, which span the observed onset time of 0715.

[53] Higher resolution (in both space and time) images of the tail B_z leading up to dipolarization are shown in Figure 17. Within a few minutes prior to substorm onset, a flux rope (as seen by the $\pm B_z$ pair indicated by the dashed lines) is seen to propagate toward the inner edge of the plasma sheet. The magnetic signature of this flux rope is limited to the plasma sheet. Above and below the plasma sheet, enhancements in positive B_z are seen to develop and accompany the flux rope into the inner edge of the plasma sheet. The effect of the earthward propagation of this structure leads to rapid dipolarization of the magnetic field of the inner magnetosphere starting at about 0257 UT, which is very close to the observed onset time. It should also be noted that these features develop in the region where there are enhanced O^+ as described in the previous section.

[54] The plots of B_z for the second substorm are shown in Figure 18. X-line reconnection is seen to be initiated between 0631 and 0646 UT, which is more than 30 min before the observed onset. The formation of a Y-line configuration where there is an extended length of negative B_z in the tail is seen to develop at about 0701 which is a few minutes prior to the observed onset. Thus, both substorms have the feature that X-line reconnections occurs well before onset, and Y-line reconnection is occurring a few tens of minutes to several minutes in front of onset.

[55] We can validate the timing of reconnection by comparing the model magnetic field with the in situ observations from Cluster as in Figure 19. The solid black lines indicate the Cluster observations while the blue line indicates the model magnetic field at Cluster's position. The dashed lines indicate the observed onset times while the dotted lines indicate the times when X-line formation occurs within the model. It should be noted that because of the dipole tilt and the orientation of the solar wind, there are small negative B_z

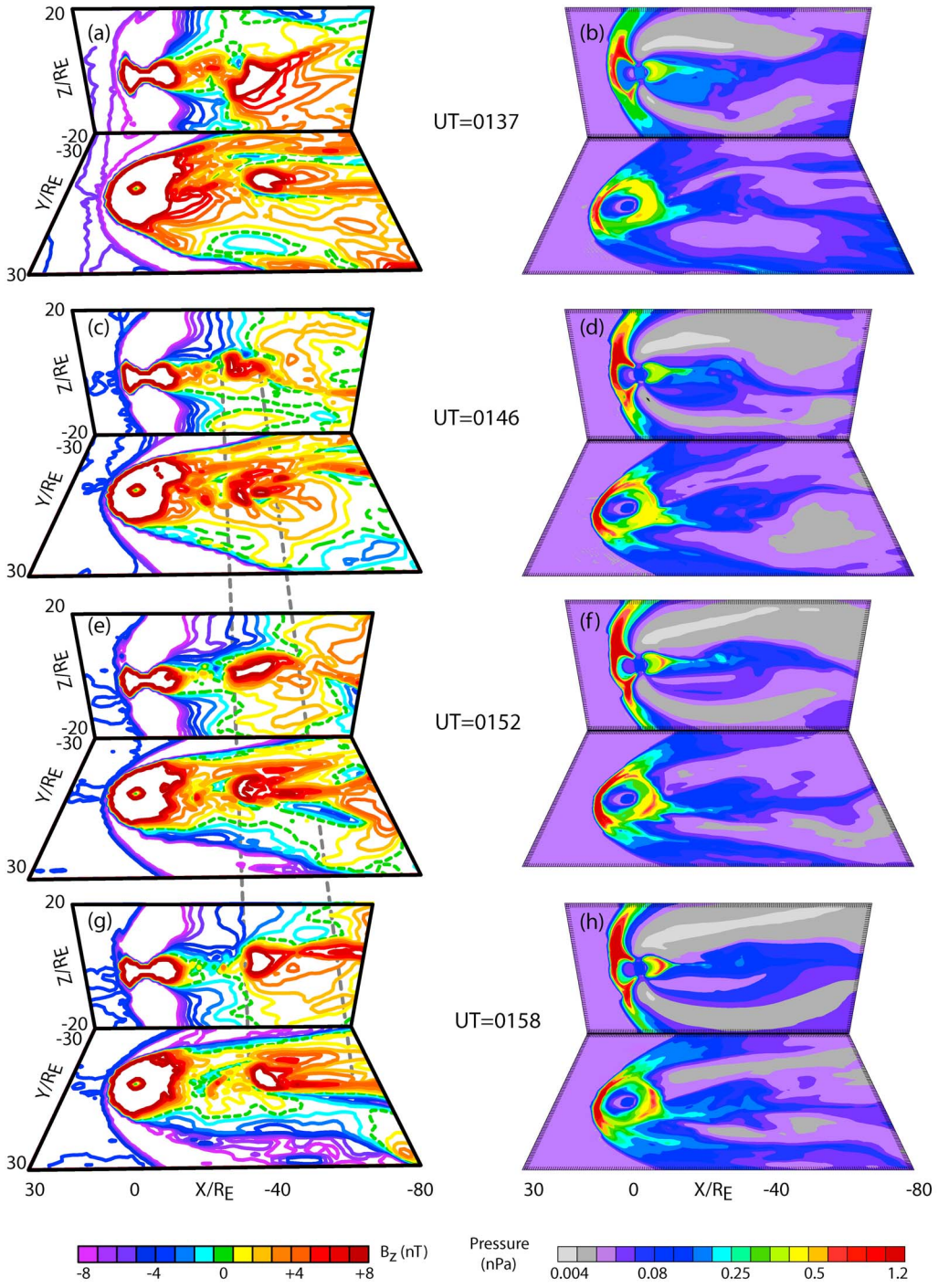

Figure 14. (left) Saturated contours of B_z showing the development of the reconnection line and (right) total plasma pressure for both the noon-midnight meridian and equatorial plane. The tail magnetic field is initial positive with reconnection across the bulk of the tail occurring around 0158 UT.

excursions in both the data and model results which are associated with the overall configuration of the tail, and are not due to reconnection processes. Only the larger −5 nT extensions should be considered as reconnection signatures. It is seen that the model is able to capture the increase in the magnitude of the lobe fields B_x, the change in orientation of B_y and the tail-like configuration in B_z up to about 0245 UT. After this time the model B_y significantly differs from the observations until 0500 UT. The differences in B_x and B_z last for a shorter time between 0245 and 0330 UT before the two results again start tracking. These differences occur because the current sheet is very thin during these times and even a small difference in position makes a large difference in the observed magnetic field.

[56] Despite these differences, the model is tracking the Cluster observations at both times when the model indicates

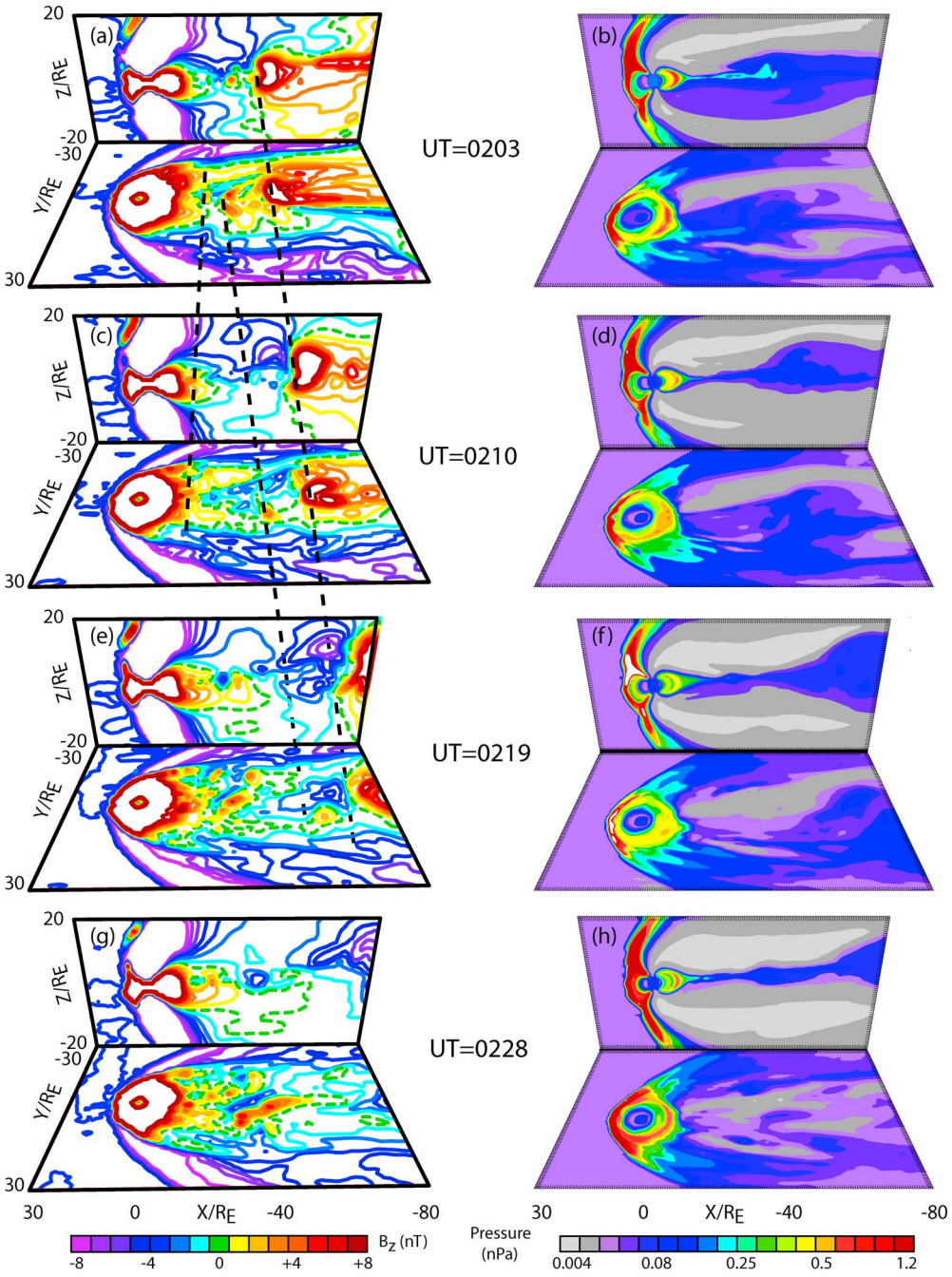

Figure 15. Continuation of Figure 14. Dashed line shows the motion of the X-line down the tail. The dusk flank of the X-line moves slower down the tail due to additional mass loading from the dawn to dusk acceleration of plasma across the tail.

that X-line reconnection is occurring earthward of Cluster's position. In addition, the Cluster data shows large negative B_z excursions approximately 15 min prior to the first substorm and between 15 and 30 min prior to the second substorm onset. These negative excursions are all accompanied by large excursions in B_y indicating that magnetic flux ropes are being observed and these flux ropes are observed before substorm onset.

[57] In order to gain a more comprehensive view of the evolution of the magnetic field, Figure 20 shows the evolution of the magnetic field at four positions along the noon-midnight meridian at ±0.5 R_E in z from the center of the current sheet. Dipolarization including a reduction in the magnitude of B_x and with B_z becoming more positive is clearly seen in the time profiles. These dipolarization signatures occur within a few minutes of the observed onset times. The strength of the dipolarization is dependent on position, with the strongest dipolarization occurring out to about 17.5 R_E for the first substorm and out to about 15 R_E for the second substorm. In addition, the very negative B_y

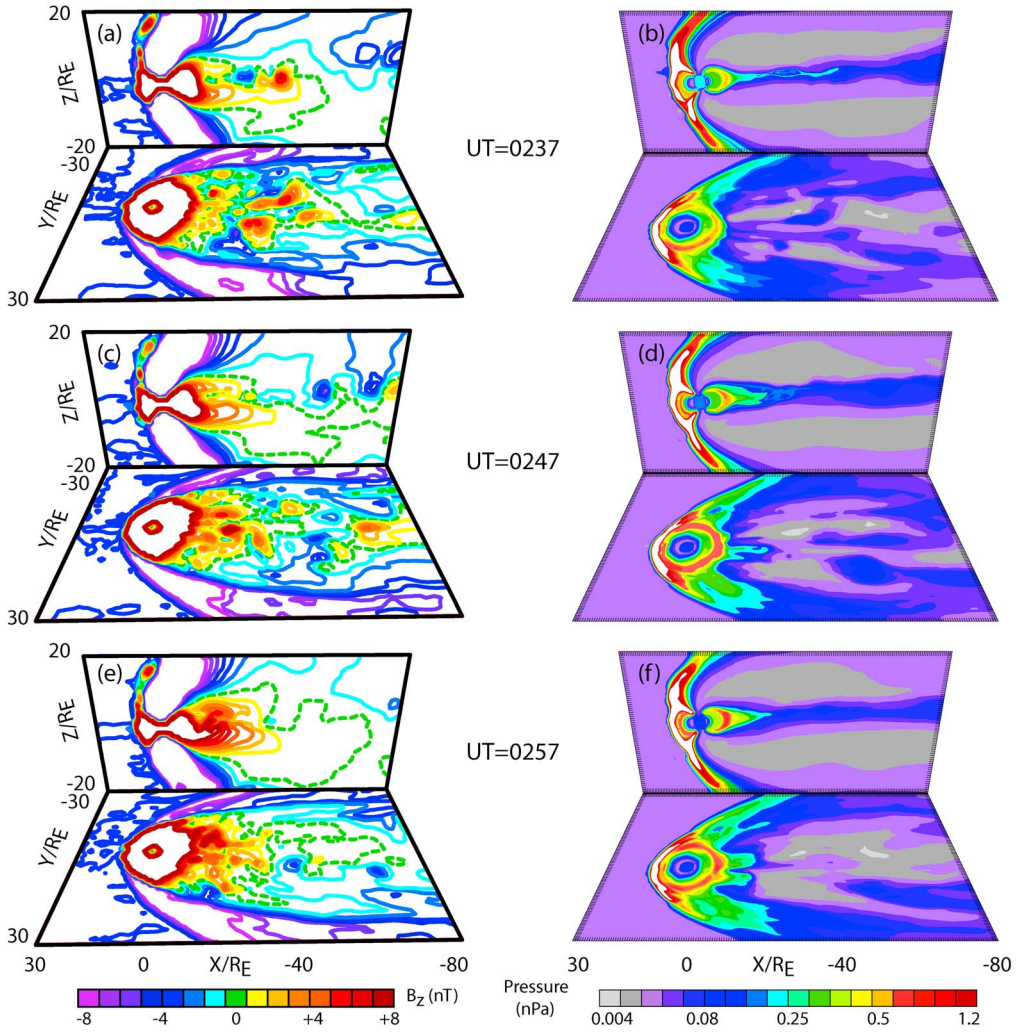

Figure 16. Continuation of Figure 15. While a thin current sheet is present up to substorm onset, reconnection in the tail is not actually occurring at substorm onset.

excursion seen in the Cluster data are captured at these positions particularly between 17.5 and 20 R_E down the tail. These negative B_y excursions span at least some of the period prior to the first substorm onset when Cluster is seeing similar distortions to B_y. Thus while the agreement between the model and observed magnetic fields is not perfect there is sufficient similarities between the two to indicated that reconnection processes are occurring well in advance of the observed substorm onsets.

7. Summary

[58] In this paper we have used multifluid/multiscale simulations to examine ionospheric influences on two substorms that were observed by Cluster on August 13, 2001. Calibration of the multifluid model with respect to observations from polar orbiting spacecraft have been undertaken in the past to quantify outflow rates as a function of MLT and MLat in addition to the total flux. The present work provides the first comparative study with tail observations with the objective of determining whether these ionospheric outflows have a significant effect on the development of magnetospheric activity.

[59] The first of these substorms occurred during increasing solar wind density and strong negative IMF B_z. The second substorm occurred under decreasing solar wind conditions and weak southward IMF B_z. The substorms were separated by more than 4 h and as such can be considered as isolated substorms. Despite the more intense IMF B_z, the first substorm has the longer growth phase of 2 h while the growth phase for the second substorm was about 1.5 h.

[60] The multifluid modeling is able to account for nearly two orders of magnitude variation in the H^+ density and one order of magnitude variation in the O^+ density observed by Cluster during the two substorms. In addition, the model results also capture the change in relative density of O^+ which can exceed 10–30% in the lobes prior to the observed onset times. These increases in O^+ relative density are in part due to an increase in O^+ reaching the tail from enhanced ionospheric outflows that are initiated during the growth phase. However, an equally important factor is that much of the ionospheric H^+ density propagates further down tail than

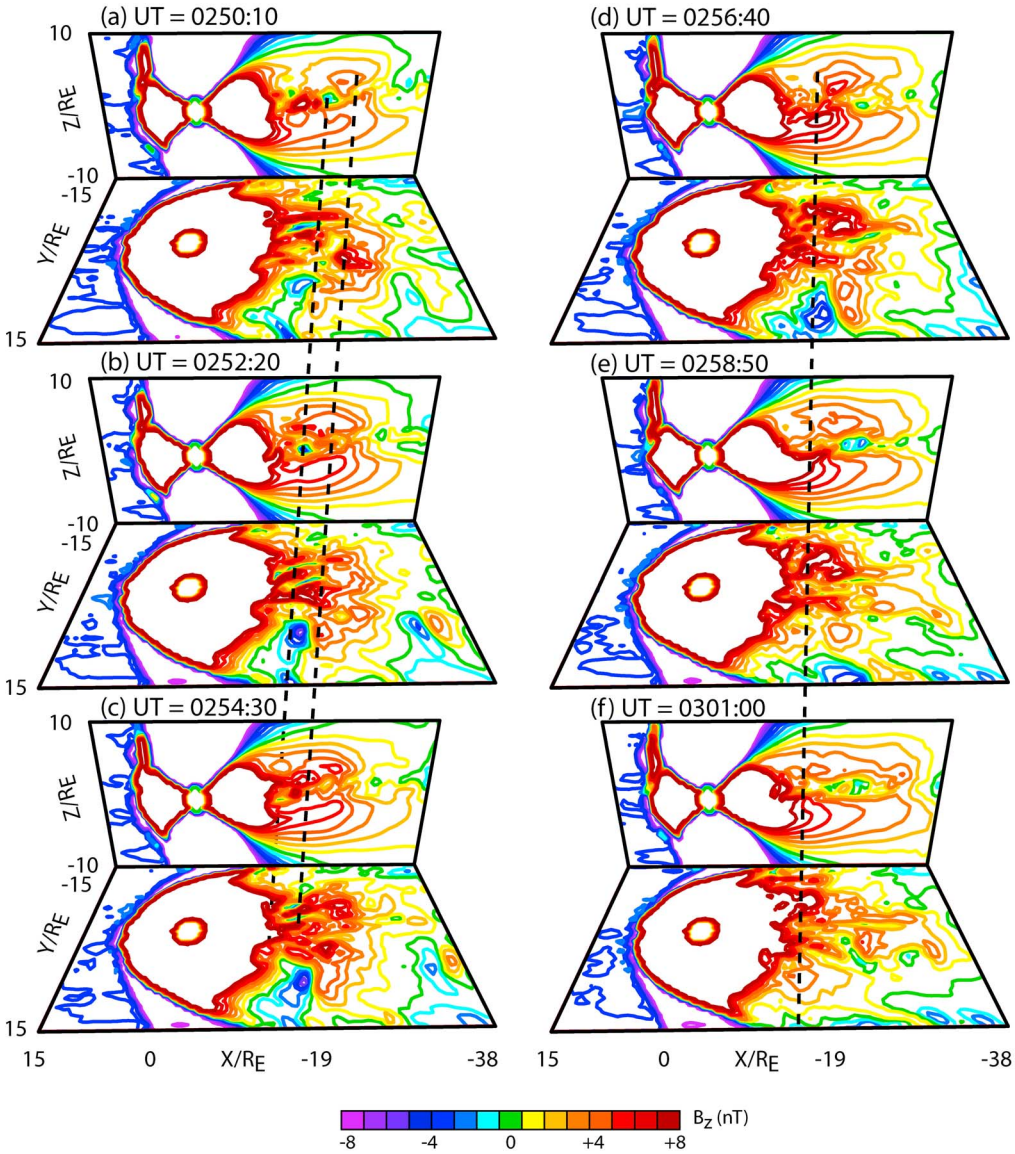

Figure 17. (a–f) The development of dipolarization in association with an earthward moving flux rope at the time of substorm onset. The earthward motion of the front is indicated by the dashed lines. From a spacecraft perspective, dipolarization would be observed after the propagation of an earthward moving flux rope ($\pm B_z$ pair) if the spacecraft were close to the center of the plasma sheet otherwise it would be associated with the observation of a region of enhanced positive B_z at further displacements from the center of the current sheet.

the O^+ ions leading to regions where the H^+ density is declining while the O^+ density is rising. These two factors contribute to the relative O^+ density reaching a few tens of percent in a time when the overall total density is decreasing. These results suggest that the changing composition of the plasma sheet plays an important role in the development of substorm dynamics.

[61] It is shown that the decline in density in the magnetotail during the growth phase is associated with the venting of solar wind plasma that had previously been entered the magnetosphere or is entering the magnetosphere during the build-up of the growth phase. This venting of solar wind plasma is associated with the formation of an X-line in a proton dominated plasma sheet [*Harnett et al.*, 2010]. A recent comparison with multifluid modeling and with in situ THEMIS data supports this sequence of events. The formation of the X-line leads to the ejection of a plasmoid at approximately 30–60 min prior to onset, similar to the idealized substorm considered by *Winglee et al.* [2009]. Since this reconnection is occurring on field lines that thread the pre-existing plasma sheet this reconnection is identified as plasma sheet reconnection. As noted by *Winglee et al.* [2009] the development of plasma sheet reconnection can drive pseudo-breakup but it has is insufficient power to drive substorm onset, and occurs too early to be considered as the trigger for onset.

[62] The need for the venting of solar wind plasma can explain the difference in duration of the growth phases of

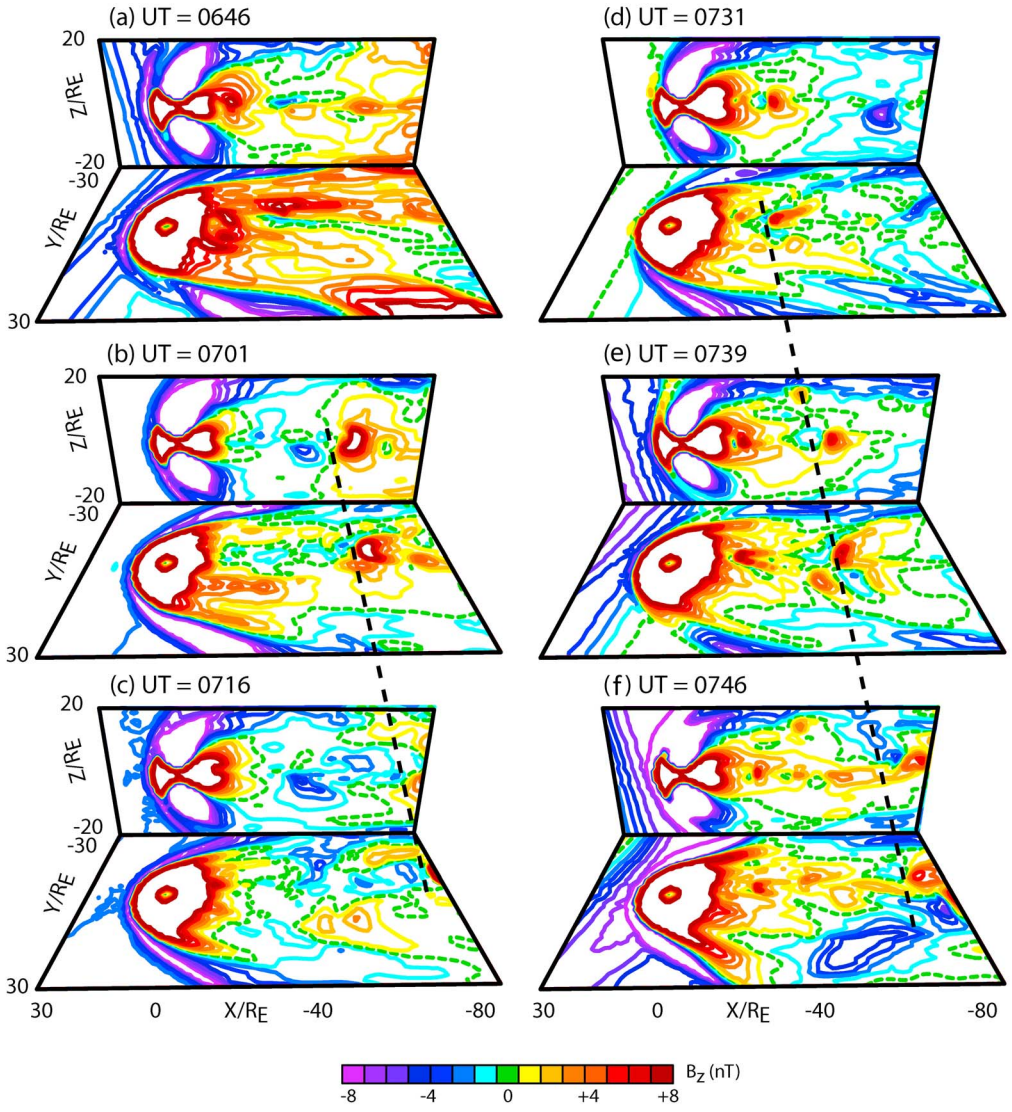

Figure 18. (a–f) Evolution of B_Z for the second substorm. X-line reconnection is initiated at 0646 UT and Y-line reconnection at about 0700 UT.

the two substorms. In the first event the incident solar wind flux is increasing. The resulting increased solar wind dynamic pressure enables more of the pre-existing solar wind plasma to reach the plasma sheet. Without this additional forcing, the solar wind plasma which enters through recently reconnected field lines on the dayside would otherwise be convected into the deep tail and not reached the near-Earth plasma sheet. Thus, solar wind access to the plasma sheet is enhanced for the first substorm causing the first substorm to have the longer growth phase. The second substorm which occurs during declining solar wind density has the shorter growth phase despite the fact that magnitude of IMF B_z is less than a third of that for the first substorm.

[63] After the plasmoid is ejected, the tail field lines are highly stretched producing a Y-configuration. Within this stretched tail, localized reconnection occurs producing the formation of flux ropes that can propagate either tailward or earthward [*Winglee et al.*, 2009]. The results here show that the reconnection in this part of the growth phase involves lobe field lines being convected into the plasma sheet. These lobe field lines have a predominantly ionospheric composition, which indicates that ionospheric outflows do in fact have an important role in the development of substorms. Of equal importance is that when this lobe reconnection is occurring in the near-Earth region, field lines that are strongly enriched in O^+ but depleted in H^+ are being convected into the plasma sheet.

[64] When this O^+ reaches the plasma sheet it experiences preferential current sheet acceleration due to the fact that its gyroradius is comparable to the current sheet thickness whereas H^+ with it smaller gyroradius have trajectories that are dominated by convective drifts. As a result of this preferential acceleration, the O^+ concentration in the plasma sheet does not increase for an isolated substorm, consistent with *Kistler et al.* [2006]. For storm-time substorms the O^+ outflow rate is higher than in the isolated substorms considered here and could potentially lead to absolute increases

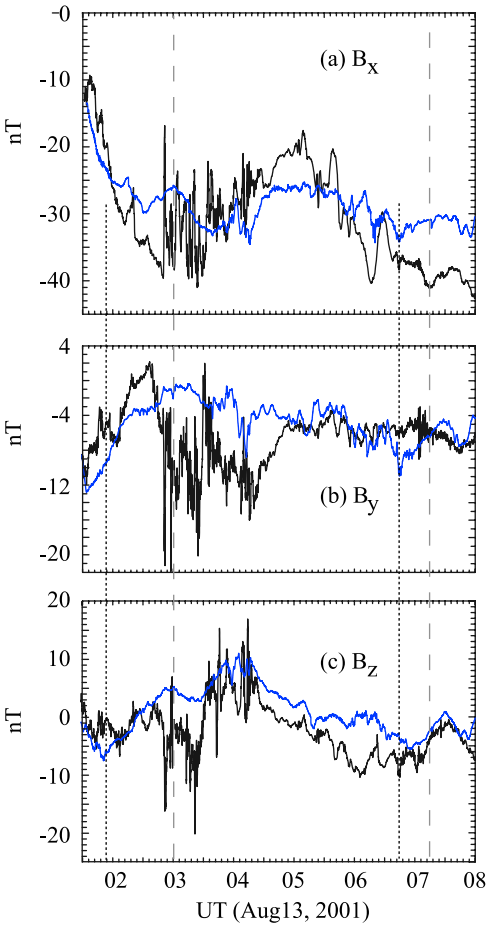

Figure 19. (a–c) Comparison of the model magnetic field (blue line) with the observed magnetic field at Cluster (black line). The long dashed lines indicated onset times while the dotted lines show the initiation of X-line reconnection.

in the concentration of O^+ in the plasma sheet for storm-time substorms.

[65] Nevertheless, the feeding of O^+ enriched lobe field lines into the plasma sheet has two important effects. First, it leads to an increase in the energy dissipation within the current sheet as energy is more efficiently transferred to the heavy ions. Second, this energized O^+ is directed into the inner edge of the plasma sheet and leads to the rapid build up of an over pressure at the inner edge of the plasma sheet. The propagation of earthward moving flux ropes which might be interpreted as a dipolarization front will aid in the rapid buildup of the pressure at the inner edge of the plasma sheet. The model results show that O^+ can contribute to nearly 50% of the total pressure at the inner edge of the plasma sheet just prior to the observed onset times. This rapid buildup leads to an over pressure that can no longer be confined by the plasma sheet currents leading to dipolarization of the magnetic field. The timing of this dipolarization is within minutes of the observed onset times for both substorms, implying that the buildup of energized O^+ at the inner edge plasma sheet is an important factor in the triggering of onset. These results suggest that there is an important relationship between substorm onset and heavy ionospheric outflows that has been overlooked to date.

[66] Our results provide a natural explanation why lobe reconnection and not plasma sheet reconnection is important in determining substorm onset. Plasma sheet reconnection primarily involves an H^+ dominated plasma while lobe reconnection involves field lines that are substantially enriched in O^+ heavy ions which modify the dissipation rate in the current sheet and the deposition rate at the inner edge of the plasma sheet.

[67] Future work needs to fully generalize the above conclusions for externally triggered substorms and storm-time substorms. However, the above scenario for onset provides a natural explanation as to why different substorms have different lengths of growth phases which cannot be explained solely by the strength of the IMF B_z. Differences between isolated substorms and storm-time substorms also need to be

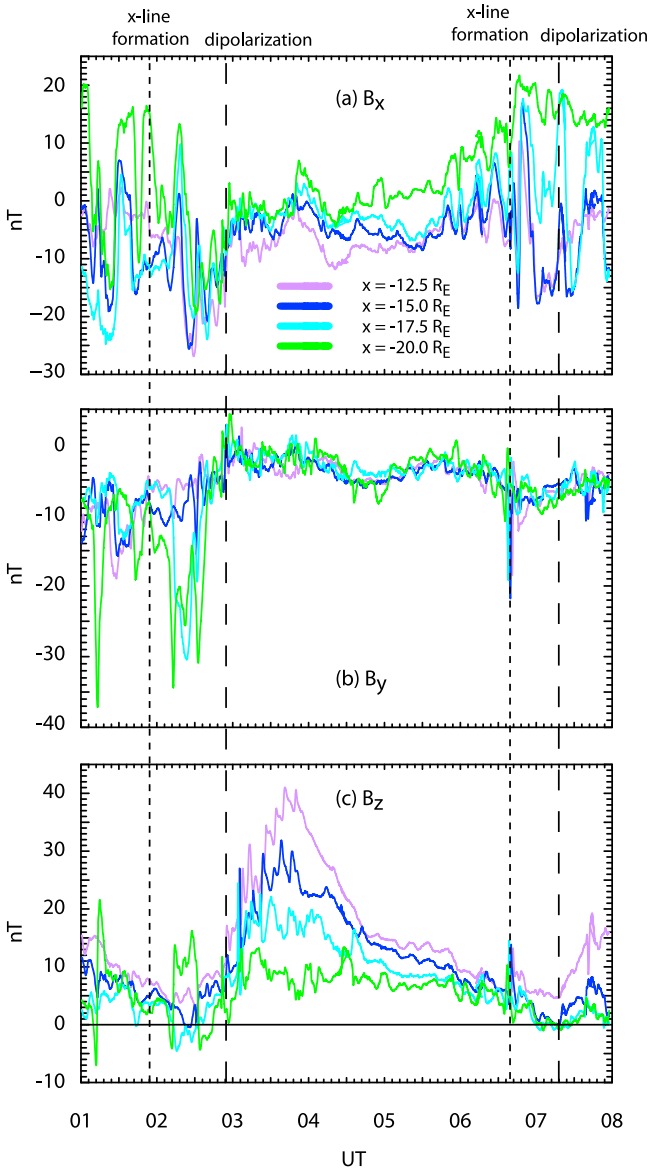

Figure 20. (a–c) Magnetic signatures along the length of the tail. The long dashed lines indicated onset times while the dotted lines show the initiation of X-line reconnection. The model is able to capture dipolarization as seen by increases in B_z at the observed onset time is capture.

investigated. One expected difference is that for isolated substorms the average outflow of the heavy ions is smaller than storm-time substorms so that for isolated substorms the outflow rate is insufficient to build up increased O^+ densities in the plasma sheet. With the increased outflows of O^+ during storms, O^+ concentrations can increase not only in the lobe but also in the plasma sheet, and additional changes from the dynamics of a proton dominated plasma sheet are expected to occur.

8. Conclusions

[68] The above results show that the growth phase of the storm is not only associated with the thinning of the current sheet but also the venting of solar wind plasma down the tail. Plasma sheet reconnection occurs during this period including the ejection of a large-scale plasmoid and the generation of smaller scale flux ropes. Subsequent lobe reconnection differs from this reconnection in that the composition is very different and involves flux tubes that are significantly enriched in ionospheric O^+ associated with enhanced outflows initiated during the growth phase. Because of its larger gyroradius, O^+ can be preferentially accelerated and lead to the rapid the deposition of energy at the inner edge of the plasma sheet. The deposition of this energy is aided by earthward moving flux ropes which have the standard $\pm B_z$ signature in the center of the current sheet but which have enhanced $+B_z$ in the lobes. The combination of processes leads to dipolarization associated with substorms onset. As such, ionospheric plasma and particularly O^+ play a crucial role in the development of substorms.

[69] **Acknowledgments.** The author gratefully acknowledges H. Frey and L. Kistler for providing their substorm onset databases to initiate the work described in this paper. The author wishes to acknowledge many lively and helpful discussions with W. K. Peterson. This work was supported by NASA grant NNX10AK96G to the University of Washington.

References

Ashour-Abdalla, M., M. El Alaoui, V. Peroomian, R. J. Walker, L. M. Zelenyi, L. A. Frank, and W. R. Paterson (1999), Localized reconnection and substorm onset on Dec. 22, 1996, *Geophys. Res. Lett.*, *26*, 3545, doi:10.1029/1999GL003630.

Baker, D. N., E. W. Hones, D. T. Young, and J. Birn (1982), The possible role of ionospheric oxygen in the initiation and development of plasma sheet instabilities, *Geophys. Res. Lett.*, *9*, 1337, doi:10.1029/GL009i012p01337.

Baker, D. N., T. I. Pulkkinen, V. Angelopoulos, W. Baumjohann, and R. L. McPherron (1996), Neutral line model of substorms: Past results and present view, *J. Geophys. Res.*, *101*, 12,975, doi:10.1029/95JA03753.

Chappell, C. R., T. E. Moore, and J. H. Waite Jr. (1987), The ionosphere as a fully adequate source of the Earth's magnetosphere, *J. Geophys. Res.*, *92*, 5896, doi:10.1029/JA092iA06p05896.

Chappell, C. R., B. L. Giles, T. E. Moore, D. C. Delcourt, P. D. Craven, and M. O. Chandler (2000), The adequacy of the ionospheric source in supplying magnetospheric plasma, *J. Atmos. Sol. Terr. Phys.*, *62*, 421, doi:10.1016/S1364-6826(00)00021-3.

Delcourt, D. C., C. R. Chappell, T. E. Moore, and J. H. Waite Jr. (1989), A three-dimensional numerical model of ionospheric plasma in the magnetosphere, *J. Geophys. Res.*, *94*, 11,893, doi:10.1029/JA094iA09p11893.

Delcourt, D. C., J. A. Sauvaud, and T. E. Moore (1993), Polar wind ion dynamics in the magnetotail, *J. Geophys. Res.*, *98*, 9155, doi:10.1029/93JA00301.

Frey, H. U., S. B. Mende, V. Angelopoulos, and E. F. Donovan (2004), Substorm onset observations by IMAGE-FUV, *J. Geophys. Res.*, *109*, A10304, doi:10.1029/2004JA010607.

Grande, M., C. H. Perry, A. Hall, J. Fennell, R. Nakamura, and Y. Kamide (2003), What is the effect of substorms on the ring current ion population during a geomagnetic storm?, in *Disturbances in Geospace: The Storm-Substorm Relationship*, *Geophys. Monogr. Ser.*, vol. 142, edited by A. S. Sharma, Y. Kamide, and G. S. Lakahini, p. 75, AGU, Washington, D. C.

Harnett, E. M., and R. M. Winglee (2003), 2.5-D fluid simulations of the solar wind interacting with multiple dipoles on the surface of the Moon, *J. Geophys. Res.*, *108*(A2), 1088, doi:10.1029/2002JA009617.

Harnett, E. M., and R. M. Winglee (2007), High-resolution multi-fluid simulations of the plasma environment near the Martian magnetic anomalies, *J. Geophys. Res.*, *112*, A05207, doi:10.1029/2006JA012001.

Harnett, E. M., R. M. Winglee, and P. A. Delamere (2005), Three-dimensional multi-fluid simulations of Pluto's magnetosphere: A comparison to 3D hybrid simulations, *Geophys. Res. Lett.*, *32*, L19104, doi:10.1029/2005GL023178.

Harnett, E. M., R. M. Winglee, and C. Paty (2006), Multi-scale/multi-fluid simulations of the post plasmoid current sheet in the terrestrial magnetosphere, *Geophys. Res. Lett.*, *33*, L21110, doi:10.1029/2006GL027376.

Harnett, E. M., R. M. Winglee, A. Stickle and G. Lu (2008), Prompt ionospheric/magnetospheric responses for the 29 October 2003 Halloween storm: Outflow and energization, *J. Geophys. Res.*, *113*, A06209, doi:10.1029/2007JA012810.

Harnett, E. M., R. M. Winglee, and T. Lerud (2010), Multiscale-multifluid simulations of the 26 February 2008 substorm: Evidence for internally triggering of a substorm, *J. Geophys. Res.*, *115*, A12238, doi:10.1029/2010JA015672.

Hirahara, M., T. Mukai, T. Terasawa, S. Machida, Y. Saito, T. Yamamoto, and S. Kokubun (1996), Cold dense ion flows with multiple components observed in the distant tail lobe by Geotail, *J. Geophys. Res.*, *101*, 7769, doi:10.1029/95JA03165.

Hones, E. W., Jr. (1984) Plasma sheet behavior during substorms, in *Magnetic Reconnection in Space and Laboratory Plasmas*, *Geophys. Monogr. Ser.*, vol. 30, edited by E. W. Hones Jr., p. 178, AGU, Washington, D. C.

Kelley, M. C. (1989), *The Earth's Ionosphere, Plasma Physics and Electrodynamics*, Academic, New York.

Kistler, L. M., et al. (2006), Ion composition and pressure changes in storm time and nonstorm substorms in the vicinity of the near-Earth neutral line, *J. Geophys. Res.*, *111*, A11222, doi:10.1029/2006JA011939.

Korth, H., R. H. W. Friedel, F. Frutos-Alfaro, C. G. Mouikis, and Q. Zong (2002), Ion composition of substorms during storm-time and non-storm-time periods, *J. Atmos. Sol. Terr. Phys.*, *64*, 561, doi:10.1016/S1364-6826(02)00013-5.

Li, Q., R. M. Winglee, M. Wilber, L. Chen, and G. Parks (2000), The geopause in relation to the plasma sheet and low-latitude boundary layer: Comparison between Wind observations and multifluid simulations, *J. Geophys. Res.*, *105*, 2563, doi:10.1029/1999JA900369.

Lotko, W. (2007), The magnetosphere-ionosphere system from the perspective of plasma circulation: A tutorial, *J. Atmos. Sol. Terr. Phys.*, *69*, 191, doi:10.1016/j.jastp.2006.08.011.

Lui, A. T. Y., C.-L. Chang, A. Mankofsky, H.-K. Wong, and D. Winske (1991), A cross-field current instability for substorm expansion, *J. Geophys. Res.*, *96*, 11,389, doi:10.1029/91JA00892.

Lui, A. T. Y., K. Liou, M. Nosé, S. Ohtani, D. J. Williams, T. Mukai, K. Tsuruda, and S. Kokubun (1999), Near-Earth dipolarization: Evidence for a non-MHD process, *Geophys. Res. Lett.*, *26*, 2905, doi:10.1029/1999GL003620.

Lyon, J. G., R. E. Lopez, C. C. Goodrich, M. Wiltberger, and K. Papadopoulos (1998), Simulation of the March 9, 1995 substorm: Auroral brightening and the onset of lobe reconnection, *Geophys. Res. Lett.*, *25*, 3039, doi:10.1029/98GL00662.

Moore, T. E., M. O. Chandler, M.-C. Fok, B. L. Giles, D. C. Delcourt, J. L. Horwitz, and C. J. Pollock, (2001), Ring currents and internal plasma sources, *Space Sci. Rev.*, *95*, 555, doi:10.1023/A:1005264907107.

Mukai, T., M. Hirahara, S. Machida, Y. Saito, T. Terasawa, and A. Nishida (1994), Geotail observation of cold ion streams in the medium distance magnetotail lobe in the course of a substorm, *Geophys. Res. Lett.*, *21*, 1023, doi:10.1029/93GL02424.

Nosé, M., A. Ieda, and S. P. Christon (2009), Geotail observations of plasma sheet ion composition over 16 years: On the variations of average plasma ion mass and O^+ triggering substorm model, *J. Geophys. Res.*, *114*, A07223, doi:10.1029/2009JA014203.

Ohtani, S., R. Yamaguchi, M. Nosé, H. Kawano, M. Engerbretson, and K. Yumoto (2002), Quiet time magnetotail dynamics and their implications for the substorm trigger, *J. Geophys. Res.*, *107*(A2), 1030, doi:10.1029/2001JA000116.

Paty, C., and R. M. Winglee (2004), Multi-fluid simulations of Ganymede's magnetosphere, *Geophys. Res. Lett.*, *31*, L24806, doi:10.1029/2004GL021220.

Paty, C., and R. Winglee (2006), The role of ion cyclotron motion at Ganymede: Magnetic field morphology and magnetospheric dynamics, *Geophys. Res. Lett.*, *33*, L10106, doi:10.1029/2005GL025273.

Peterson, W. K., H. L. Collin, A. W. Yau, and O. W. Lennartsson (2001), Polar/Toroidal Imaging Mass-Angle Spectrograph observations of suprathermal ion outflow during solar minimum conditions, *J. Geophys. Res.*, *106*, 6059, doi:10.1029/2000JA003006.

Seki, K., M. Hirahara, T. Terasawa, I. Shinohara, T. Mukai, Y. Saito, S. Machida, T. Yamamoto, and S. Kokubun (1996), Coexistence of Earth-origin O^+ and solar wind-origin H^+/He^{++} in the distant magnetotail, *Geophys. Res. Lett.*, *23*, 985, doi:10.1029/96GL00768.

Seki, K., M. Hirahara, T. Terasawa, T. Mukai, Y. Saito, S. Machida, T. Yamamoto, and S. Kokubun (1998), Statistical properties and possible supply mechanisms of tailward cold O^+ beams in the lobe/mantle regions, *J. Geophys. Res.*, *103*, 4477, doi:10.1029/97JA02137.

Shay, M. A., and M. Swisdak (2004), Three-species collisionless reconnection: Effect of O^+ on magnetotail reconnection, *Phys. Rev. Lett.*, *93*, 175001, doi:10.1103/PhysRevLett.93.175001.

Wilson, G. R., D. M. Ober, G. A. Germany, and E. J. Lund (2004), Nightside auroral zone and polar cap ion outflow as a function of substorm size and phase, *J. Geophys. Res.*, *109*, A02206, doi:10.1029/2003JA009835.

Winglee, R. M. (1994), Non-MHD Influences on the magnetospheric current system, *J. Geophys. Res.*, *99*, 13,437, doi:10.1029/94JA00260.

Winglee, R. M. (2000), Mapping of ionospheric outflows into the magnetosphere for varying IMF conditions, *J. Atmos. Sol. Terr. Phys.*, *62*, 527, doi:10.1016/S1364-6826(00)00015-8.

Winglee, R. M. (2003), Circulation of ionospheric and solar wind particle populations during extended southward IMF, *J. Geophys. Res.*, *108*(A10), 1385, doi:10.1029/2002JA009819.

Winglee, R. M. (2004), Influence of heavy ion outflows on tail reconnection and the auroral current system, *J. Geophys. Res.*, *109*, A09206, doi:10.1029/2004JA010385.

Winglee, R. M., S. Kokubun, R. P. Lin, and R. P. Lepping (1998), Flux rope structures in the magnetotail: Comparison between Wind/Geotail observations and global simulations, *J. Geophys. Res.*, *103*, 135, doi:10.1029/97JA02415.

Winglee, R. M., D. Chua, M. Brittnacher, G. K. Parks, and G. Lu (2002), Global impact of ionospheric outflows on the dynamics of the magnetosphere and cross-polar cap potential, *J. Geophys. Res.*, *107*(A9), 1237, doi:10.1029/2001JA000214.

Winglee, R. M., W. Lewis, and G. Lu (2005), Mapping of the heavy ion outflows as seen by IMAGE and multi-fluid global modeling for the 17 April 2002 storm, *J. Geophys. Res.*, *110*, A12S24, doi:10.1029/2004JA010909.

Winglee, R. M., W. K. Peterson, A. W. Yau, E. Harnett, and A. Stickle (2008a), Model/data comparisons of ionospheric outflow as a function of invariant latitude and magnetic local time, *J. Geophys. Res.*, *113*, A06220, doi:10.1029/2007JA012817.

Winglee, R. M., E. Harnett, A. Stickle, and J. Porter (2008b), Multiscale/multifluid simulations of flux ropes at the magnetopause within a global magnetospheric model, *J. Geophys. Res.*, *113*, A02209, doi:10.1029/2007JA012653.

Winglee, R. M., E. M. Harnett, and A. Kidder (2009), Relative timing of substorm processes as derived from multifluid/multiscale simulations: Internally driven substorms, *J. Geophys. Res.*, *114*, A09213, doi:10.1029/2008JA013750.

Yau, A. W., and M. André (1997), Source of ion outflow in the high latitude ionosphere, *Space Sci. Rev.*, *80*, 1, doi:10.1023/A:1004947203046.

E. Harnett and R. M. Winglee, Department of Earth and Space Sciences, University of Washington, Seattle, WA 98195-351310, USA. (winglee@ess.washington.edu)